

The ESO UVES/FEROS Large Programs of TESS OB pulsators*

I. Global stellar parameters from high-resolution spectroscopy

Nadya Serebriakova¹, Andrew Tkachenko¹, Sarah Gebruers^{1,2}, Dominic M. Bowman¹, Timothy Van Reeth¹, Laurent Mahy³, Siemen Burssens¹, Luc IJspeert¹, Hugues Sana¹, and Conny Aerts^{1,2,4}

¹ Institute of Astronomy, KU Leuven, Celestijnenlaan 200D, B-3001 Leuven, Belgium
e-mail: nadya.serebriakova@kuleuven.be

² Max Planck Institute for Astronomy, Königstuhl 17, 69117 Heidelberg, Germany

³ Royal Observatory of Belgium, Ringlaan 3, B-1180 Brussels, Belgium

⁴ Department of Astrophysics, IMAPP, Radboud University Nijmegen, PO Box 9010, 6500 GL Nijmegen, The Netherlands

Received ...; accepted ...

ABSTRACT

Context. Modern stellar structure and evolution theory experiences a lack of observational calibrations for the interior physics of intermediate- and high-mass stars. This leads to discrepancies between theoretical predictions and observed phenomena mostly related to angular momentum and element transport. Analyses of large samples of massive stars connecting state-of-the-art spectroscopy to asteroseismology may provide clues on how to improve our understanding of their interior structure.

Aims. We aim to deliver a sample of O- and B-type stars at metallicity regimes of the Milky Way and the Large Magellanic Cloud (LMC) galaxies with accurate atmospheric parameters from high-resolution spectroscopy, along with a detailed investigation of line-profile broadening, for future asteroseismic studies.

Methods. After describing the general aims of our two Large Programs, we develop dedicated methodology to fit spectral lines and deduce accurate global stellar parameters from high-resolution multi-epoch UVES and FEROS spectroscopy. We use the best available atmosphere models for three regimes covered by our global sample, given its breadth in terms of mass, effective temperature, and evolutionary stage.

Results. Aside from accurate atmospheric parameters and locations in the Hertzsprung-Russell diagram, we deliver detailed analyses of macroturbulent line broadening, including estimation of the radial and tangential components. We find that these two components are difficult to disentangle from spectra with signal-to-noise ratios below 250.

Conclusions. Future asteroseismic modelling of the deep interior physics of the most promising stars in our sample will improve the existing dearth of such knowledge for large samples of OB stars, including those of low metallicity in the LMC.

Key words. stars: fundamental parameters – stars: massive – stars: early-type – stars: rotation – asteroseismology – stars: oscillations

1. Introduction

The field of stellar astrophysics has been revolutionized with the advent of space missions such as CoRoT (Auvergne et al. 2009), Kepler/K2 (Borucki et al. 2010), and TESS (Ricker et al. 2015). This revolution became possible thanks to the high duty-cycle, nearly uninterrupted, and unprecedently long (from about a month in a single TESS sector to four years for the entire *Kepler* nominal mission duration) photometric time series at the sub-mmag level of precision that these missions delivered. This high precision data is currently available for tens of thousands of stars. These ensembles provide stringent tests for the theories of stellar structure, evolution, atmospheres, tidal interactions, etc. In particular, numerous recent studies point to both severe and less critical deficiencies in the above-mentioned theories, notably on angular momentum transport and on chemical mixing. Some of the deficiencies remain unresolved, whereas others are currently being tackled in detail from theoretical improvements (e.g., Mosser et al. 2012; Beck et al. 2012; Fuller & Lai 2012; Cantiello et al. 2014; Deheuvels et al. 2016; Fuller 2017; Fuller

et al. 2017; Hekker & Christensen-Dalsgaard 2017; Aerts et al. 2019; Bowman 2020; Deheuvels et al. 2020; Aerts 2021; Southworth 2021).

The field of binary stars is among those that received a major boost in recent years. This is in part associated with the superior quality of the space-based photometry when compared to its ground-based counterpart. It is also due to synergies enabled by various types of intrinsic variability often observed in one or both binary components. This way, solid observational detections of tidally-induced pulsations were reported in the HD 174884 system observed by CoRoT (Maceroni et al. 2009), followed by the discovery of high-amplitude tidally-induced oscillations in the *Kepler* object of interest KOI-54 (Welsh et al. 2011). KOI-54's observed properties were subsequently modelled by Fuller & Lai (2012). Numerous binary systems with stellar pulsations that are either induced or perturbed by tides have been meanwhile found and modelled (e.g., Bowman et al. 2019b; Guo et al. 2019; Handler et al. 2020; Kurtz et al. 2020; Fuller et al. 2020; Fuller 2021; Rappaport et al. 2021; Lee 2021; Van Reeth et al. 2022; Jayaraman et al. 2022). Applications occur most notably for the class of highly eccentric systems dubbed “heart-beat stars” (e.g., Thompson et al. 2012; Hambleton et al. 2013; Beck et al. 2012; Hambleton et al. 2016; Guo

* Based on observations collected at the European Southern Observatory, Chile under programs 1104.D-0230 and 0104.A-9001

et al. 2020; Cheng et al. 2020; Kołaczek-Szymański et al. 2021). Furthermore, a sample of low- and intermediate-mass binaries observed by *Kepler* has enabled empirical tests of state-of-the-art tidal evolution theory (Zahn 2013) with respect to its predictions for the circularisation of binary orbits (Van Eylen et al. 2016). Ultimately, (eclipsing) binary stars allow us to constrain the amount of core-boundary mixing and the convective core masses in intermediate- and high-mass stars (e.g., Claret & Torres 2018, 2019; Tkachenko et al. 2020; Johnston 2021, and references therein), thanks to the unique property of eclipsing, spectroscopic double-lined binaries delivering masses and radii with precision and accuracy reaching 1% level, and in some cases even better (e.g., Maxted & Hutcheon 2018; Maxted et al. 2020; Mahy et al. 2020a,b; Serenelli et al. 2021; Pavlovski et al. 2022).

Yet another field in stellar astrophysics that advances enormously with the launch and operations of space-based missions is asteroseismology. This field exploits the fact that, as stars evolve and cross different regions in the Hertzsprung-Russell (HR) diagram, they become unstable to pulsations. Two principle types of stellar pulsations are distinguished following their dominant restoring force: pressure (p) modes which are acoustic waves dominantly restored by pressure gradients, and gravity (g) modes restored by buoyancy. While p modes are typically confined to the envelope of stars, g modes have their largest amplitudes in the near-core regions and are therefore most sensitive to the physical conditions in the deep stellar interior. One of the outstanding observational findings of space-based missions is that the vast majority of stars are intrinsically variable, and that pulsating stars are found everywhere across the HR diagram (Aerts 2021; Kurtz 2022).

Asteroseismology probing the near-core region in intermediate- to high-mass stars (spectral types early-F to late-O) had to await space-based observations, owing to the long periods of their g modes (of the order of a day). Theoretically predicted informative series of (quasi-)uniformly spaced g -mode periods dubbed period spacing patterns (Miglio et al. 2008; Bouabid et al. 2013) were only recently detected from space-based photometric observations of B- and F-type stars (e.g., Van Reeth et al. 2015a,b; Pápics et al. 2017; Szewczuk et al. 2021). Detailed asteroseismic modelling of the period spacing patterns enables probes of the level and functional form of convective core boundary and envelope mixing (e.g., Moravveji et al. 2015, 2016; Szewczuk & Daszyńska-Daszkiewicz 2018; Michelsen et al. 2019, 2021; Momberg et al. 2019, 2021; Pedersen et al. 2018, 2021; Pedersen 2022; Bowman & Michelsen 2021; Szewczuk et al. 2022), internal rotation (e.g., Triana et al. 2015; Van Reeth et al. 2016, 2018; Ouazzani et al. 2017, 2020; Li et al. 2020), the physics of radiative levitation (Deal et al. 2016, 2017; Momberg et al. 2020, 2022), and impact of magnetism (Buysschaert et al. 2018; Lecanet et al. 2022) in these stars. In particular, these and other studies lead to the conclusion that standard stellar structure and evolution models of intermediate and high-mass stars incorrectly predict their convective core masses (e.g., Johnston 2021, and references therein) and lack mechanism(s) of efficient angular momentum transport already in their longest and most stable main-sequence stage of evolution (e.g., Aerts et al. 2017a, 2019; Aerts 2021, and references therein). These conclusions for the main sequence are in agreement with both observational and numerical studies of intermediate-mass stars in post-main sequence stages (e.g., Mosser et al. 2012; Beck et al. 2012; Cantiello et al. 2014; Hermes et al. 2017; Aerts et al. 2019).

Typically space-based photometry in tandem with ground-based spectroscopy reveal pulsators in regions in the HR diagram

where they were not expected. On the other hand, no signatures of pulsations are sometimes found in stars that are expected to pulsate according to their location in the HR diagram. For example, recent studies of A- and F-type stars based on *Kepler* and Gaia photometric data reveal a considerable fraction of pulsators outside of their respective theoretical instability regions (e.g., Uytterhoeven et al. 2011; Bowman & Kurtz 2018; Murphy et al. 2019; Gaia Collaboration et al. 2022). On the other hand, Balona (2014); Balona et al. (2015) report that at least 50% of A-type stars do not pulsate while being located within the borders of the theoretical instability strips. Furthermore, Balona & Ozuyar (2020) find a group of B-type stars pulsating in high-frequencies while being too cool to be explained as rapidly rotating β Cep-type p-mode pulsators whose effective temperature is substantially affected by gravity darkening. Such stars are found in both ground-based and space-based high-cadence photometry and are rather interpreted as Slowly Pulsating B (SPB) stars whose observed (prograde) g -mode frequencies are shifted to high-frequencies, sometimes above $\sim 3 \text{ d}^{-1}$, by the influence of the Coriolis acceleration on the modes and by the Doppler effect (Aerts & Kolenberg 2005; Saesen et al. 2010, 2013; Mowlavi et al. 2013, 2016; Moździerski et al. 2014, 2019; Sharma et al. 2022; Gebruers et al. 2022; Gaia Collaboration et al. 2022). This interpretation is in agreement with the theoretical computations by Bouabid et al. (2013); Salmon et al. (2014).

Stars of spectral type O and B were under-represented in the nominal *Kepler* field as its selection was dictated by the mission's core science of detecting exoplanets orbiting solar-type stars. Moreover, models of these intermediate- to high-mass stars are most uncertain among those in stellar evolution computations (e.g., Martins & Palacios 2013). This current state of affairs motivates us to look closely at photometric data delivered by the all-sky TESS mission as its observational strategy does not bias against O and B stars, and allows us to target these objects both in the Milky Way and Large Magellanic Cloud (LMC) galaxies. The LMC is a challenging laboratory for the theory of heat-driven stellar pulsations as it depends strongly on the metallicity. The lower value of metallicity of the LMC and its implied low number of predicted pulsators is therefore of particular interest (cf., Salmon et al. 2014). Preliminary investigations of TESS data of massive stars in the LMC indeed indicate few heat-driven pulsators (Bowman et al. 2019a).

The current paper is the first one in a series aiming at a full application of asteroseismology to O and B stars, from a combined approach using space photometry and astrometry together with high-resolution spectroscopy. As is necessarily the case in massive stars asteroseismology, by nature of those stars' oscillation characteristics, it concerns a long-term project and the overall study involves several (PhD) sub-projects. Here, we first present the overall project aims and subsequently focus on the derivation of the global spectroscopic parameters of the target stars, which were selected from Cycle 1 TESS space-based photometry. In Sect. 2, we present the concrete scientific motivation, the role of TESS space-based photometry, the asteroseismic quantities we are after, the role of the ESO high-resolution ground-based spectroscopy in our Large Programs, and the sample selection. The spectroscopic observations and custom data processing are described in Sect. 3, while spectroscopic classification, inference of atmospheric parameters, and investigation of line broadening mechanisms in the spectra of the sample stars are detailed in Sect. 4.

We provide a detailed discussion of the obtained results, keeping in mind the photometric classification of stars from Cycle 1 TESS photometry, and conclude the paper in Sect. 6. Sub-

sequent papers will tackle abundance determinations, frequency analyses from the full Cycle 1 to Cycle 4 TESS photometric light curves, and stellar modelling for all O and B pulsators with sufficient identified modes based on all observational input, including all the Gaia data that will be available at that stage of our project.

2. Two ESO Large Programs with the FEROS and UVES spectrographs

2.1. The overall project goals

The ultimate goal of our two ESO large programs (UVES: 1104.D-0230; FEROS: 0104.A-9001) is to remedy the current lack of a high-precision observational calibration for the theoretical description of stellar interiors in stellar structure and evolution models of intermediate- to high-mass stars. Our concrete goals can only be achieved by exploiting complementary (ESO) high-resolution spectroscopy along with TESS space-based photometry and Gaia astrometry for a wide range of stellar masses covered by OB(AF)-type stars.

With our two large programs, we aim to (i) resolve the current two-orders-of-magnitude discrepancies between theory and observations of angular momentum transport; (ii) deliver asteroseismically calibrated mixing profiles for stellar interiors, which currently do not exist in a quantitative sense for high-mass stars and are scarce for intermediate-mass stars; (iii) challenge state-of-the-art models of stellar structure and pulsations by searching for coherent g-mode pulsators in the low-metallicity regime of the LMC; and (iv) investigate possible connections between coherently and/or stochastically excited gravity waves and turbulent velocity fields in the atmospheres of OB stars. Furthermore, our program is designed in such a way as to enable an observational check for binarity, which also allows us to deliver an unprecedented legacy for future studies of pulsators in (close) binaries. Tidal asteroseismology is capable of quantifying the effect of tides by investigating the internal rotation and mixing in close binaries and comparing the outcome to the single-star case (e.g., Guo 2021; Lampens 2021, for reviews).

2.2. Asteroseismology of massive stars: the role of TESS

Unlike “classical” observational methods (for example, snapshot spectroscopy and multi-colour photometry) that largely concern surface properties of stars, asteroseismology offers insight into the internal physics of stars through the interpretation of detected and identified stellar oscillations. Hence it is an optimal tool to evaluate and calibrate models of stellar interiors, provided that we can detect and identify sufficient modes in terms of their l , m , and n numbers (Aerts et al. 2010a).

In terms of angular momentum transport in intermediate-mass dwarfs, the asteroseismic ensemble studies by Van Reeth et al. (2016, 2018); Aerts et al. (2017b); Ouazzani et al. (2019) demonstrate that stars born with a convective core tend to show almost rigid rotation in their radiative envelopes independent of their near-core rotation rate and evolutionary stage. This implies that strong coupling between the convective core and radiative envelope occurs on the main sequence. This conclusion is based on studies of stars with mass between $1.3 M_{\odot}$ and $9 M_{\odot}$, with the mass distribution being largely skewed towards late-B and F-type stars ($M \lesssim 3.0 M_{\odot}$). Only for this mass regime, the later evolutionary stages have been mapped in great detail (e.g., Aerts et al. 2019, for a review). The goal of our ESO UVES+FEROS large programs is to expand the parameter space towards the higher stellar mass regime ($M \gtrsim 3.0 M_{\odot}$) by focusing on stars of

spectral type O and B on the main sequence, as well as in the hydrogen-shell and core-helium burning phases covered by blue supergiants. These phases constitute ~90% of the total lifetime of massive stars, excluding the remaining short period prior to the remnant formation when considerable mass loss occurs due to a radiation- or dust-driven wind. During this final phase, unambiguous detections of modes is challenging due to the strong wind.

Previously, analyses of the CoRoT and *Kepler*/K2 photometric data revealed the presence of non-radial oscillation modes in core-hydrogen burning stars with masses between 3 and $\sim 25 M_{\odot}$ (e.g., Neiner et al. 2009; Huat et al. 2009; Diago et al. 2009; Gutiérrez-Soto et al. 2009; Degroote et al. 2010a; Briquet et al. 2011; Mahy et al. 2011; Thoul et al. 2013; Buyschaert et al. 2015; Pápics et al. 2017; Szewczuk et al. 2021; Pedersen et al. 2021) and in blue supergiants (Aerts et al. 2010b, 2017a, 2018; Simón-Díaz et al. 2018). Forward asteroseismic modelling is only available for about 30 of them, with quite different levels of depth (Aerts et al. 2011; Briquet et al. 2011; Neiner et al. 2012; Moravveji et al. 2015, 2016; Michelsen et al. 2021; Pedersen et al. 2021). The majority of the other intermediate-to-high mass pulsators lack proper mode identification, particularly for those with short light curves (less than half a year). Prior to space asteroseismology, long-term ground-based campaigns did already lead to such modelling for a few bright β Cep stars, yet based on only a few identified modes (Aerts et al. 2003; Handler et al. 2006; Dziembowski & Pamyatnykh 2008; Handler et al. 2009; Briquet et al. 2012).

CoRoT data gave rise to the detection of stochastic high-frequency oscillations in a few OB-type stars (Belkacem et al. 2009; Degroote et al. 2010b), driven by either turbulent envelope convection (Belkacem et al. 2010) or nonlinear resonant mode coupling (Degroote et al. 2009). Moreover, Blomme et al. (2011) found stochastic low-frequency (SLF) variability in the CoRoT data of several rapidly-rotating O-type stars. Such SLF was later found to be present, often in addition to coherent oscillation modes, for the vast majority of O and B stars observed with CoRoT or K2 (Bowman et al. 2019).

A similar discovery was made for a sample of some 50 LMC O- and B-type stars observed with TESS (Bowman et al. 2019a). The lack of dependence of the properties of SLF variability on the metallicity of the star and its apparent scaling with the stellar (convective core) luminosity led to the interpretation that internal gravity waves (IGWs) excited stochastically at the core boundary are the cause of the observed photospheric variability (see, e.g., Rogers et al. 2013; Edelmann et al. 2019; Ratnasingam et al. 2020; Horst et al. 2020), although alternative interpretations have also been suggested (Lecocanet et al. 2019). In any case, SLF variability is ubiquitous in OB stars and is related to their mass and age (Bowman et al. 2020).

In conclusion, too few O- and B-type pulsators have been modelled in sufficient asteroseismic depth to improve the physics of stellar interiors for stars with masses above $\sim 5 M_{\odot}$ (Bowman 2020). This is why we resort to the TESS mission, offering hundreds of potential massive candidate pulsators with high-cadence photometry covering at least 6 months of uninterrupted light curves, following our approved TESS guest observer programs covering cycles 1 to 5 of the extended mission (PI Bowman¹).

¹ <https://heasarc.gsfc.nasa.gov/docs/tess/approved-programs.html>

2.3. The quest for mixing and rotation profiles

Because coherent g-modes and stochastically excited IGWs are both confined to the low-frequency regime (typically below some 3 d^{-1} or $\sim 35 \mu\text{Hz}$), while asteroseismic analyses require individual pulsation modes to be resolved, our goals can only be achieved by exploiting TESS light curves of longer duration than the CoRoT light curves. Therefore, we focus on OB stars in the Southern Continuous Viewing Zone (CVZ-S) of TESS and its vicinity – the regions of the sky that have between some 200 d and 1-yr long, high duty cycle photometric data, which is long enough to enable both p- and g-mode asteroseismology. We take an observationally driven approach with the goal to estimate the following three quantities for a representative sample of single intermediate- and high-mass stars from their asteroseismic analysis: (i) $\Omega(r, t)$ - the interior rotation frequency and its evolution in time, (ii) $D_{\text{ov}}(r, t)$ - the convective core overshooting profile and its evolution in time, and (iii) $D_{\text{mix}}(r, t)$ - the chemical mixing profile in the radiative envelope and its evolution in time. Here, t is the age of the star and $r \in [0, R(t)]$ is the depth inside the star from the centre $r = 0$ to the surface at $r = R(t)$. The quantity $D_{\text{mix}}(r, t)$ captures the cumulative effect of all active mixing phenomena in the radiatively stratified envelope from the star's birth until t .

With an addition of the four minimum free parameters that are required to compute evolutionary models, namely the stellar mass M , the initial hydrogen and metal mass fractions (X, Z), and the age t , asteroseismology turns out to be at least a 7D problem, even in the simplest case where the three above mentioned internal profiles would only have one free parameter that does not change in time. However, as shown by Van Reeth et al. (2016) this 7D estimation problem can be broken down into a multi-step approach. In particular, interpretation of the period spacing patterns of g modes (cf. Sect. 1) allows us to estimate the near-core rotation frequency of the star, Ω_{core} (Van Reeth et al. 2016; Ouazzani et al. 2017; Li et al. 2020). Furthermore, the inclusion of envelope mixing $D_{\text{mix}}(r)$ appreciably affects high-order g modes and it determines the surface abundances of CNO-produced chemical elements. In addition, g modes are capable of differentiating between different $D_{\text{ov}}(r)$ profiles for main-sequence stars (Pedersen et al. 2018, 2021; Pedersen 2022; Michielsen et al. 2019, 2021). This way, combined asteroseismology and surface abundances information can be used to constrain the amount and functional form of mixing in both the near-core region and radiative envelope of intermediate- to high-mass stars. Aerts et al. (2018) provided methodology for forward asteroseismic modelling encapsulating all the above-described analysis steps, relying on state-of-the-art statistical principles to account for theoretical model prediction uncertainties as well as strong correlations among the numerous free parameters to estimate.

2.4. The role of ESO high-resolution spectroscopy

High-quality spectroscopic observations are essential to address the above science questions and to meet our goals. We therefore applied for high-resolution ($R \gtrsim 40\,000$), high signal-to-noise ratio ($S/N \sim 100$) two-epoch spectroscopy for a sample of TESS O- and B-type variable stars in the Milky Way and LMC galaxies. These data were obtained with the Ultraviolet and Visual Échelle Spectrograph (UVES; Dekker et al. 2000) and the Fiber-fed Extended Range Optical Spectrograph (FEROS; Kaufer et al. 1999) instruments attached to the UT2@VLT and MPG/ESO 2.2-m telescopes, respectively.

UVES is a cross-dispersed échelle spectrograph that covers the entire optical range with its two arms (300–500 nm and 420–1100 nm in the blue and red arms, respectively) and offers a variety of spectral resolving power possibilities (up to 80 000 and 110 000 in the blue and red arm, respectively) regulated by the slit width of the instrument. We have opted for the UVES² DIC-2 blue arm standard setting (CD2, 437+760 nm) as it covers a number of Balmer (including H_α) and helium lines – the main diagnostic lines for the determination of fundamental atmospheric parameters – as well as important diagnostic lines of metals for the determination of $v \sin i$, micro- and macro-turbulent velocities, and surface abundances of OB stars. Because massive stars are typically moderate to fast rotators, we chose a slit width of 1 arcsecond, corresponding to a resolving power of $R \sim 40\,000$, which is sufficient to properly resolve individual lines in the spectra of these stars.

FEROS³ is a fiber-fed échelle spectrograph covering the wavelength range from some 350 nm to 920 nm. It operates at a resolving power of $R \sim 48\,000$. This combination of a wide wavelength range and high spectral resolution makes the instrument ideal to feed the stellar astrophysics community with high-quality spectroscopic observations of relatively bright stars, including intermediate- to high-mass stars of spectral type O and B.

2.5. Sample selection

Our sample selection was largely based on the studies of massive stars by Bowman et al. (2019a) and Pedersen et al. (2019) with respect to their photometric variability as detected in the first sector(s) of TESS data. Their samples have been complemented with a global search for stars of spectral type O and B in the Southern CVZ of TESS, using the infrastructure and functionality of the Simbad astronomical database⁴ (Wenger et al. 2000). This obtained list of OB targets has been cross-matched with the catalogues of Bowman et al. (2019a,b, 2020); Pedersen et al. (2019) and the targets that did not have a match were kept in the sample for further consideration. For these extra targets, we have performed custom extraction of their light curves from the TESS Full Frame Images (FFIs) and performed their visual photometric variability classification based on the dominant signal detected in the TESS data. All eclipsing binaries have been excluded, making our sample biased against this type of objects — TESS (pulsating) eclipsing binaries constitute a separate (PhD) study (cf., IJspeert et al. 2021). This way, we ended up with slightly over 350 targets that were prioritised according to their potential for future asteroseismic modelling. All stars were subjected to a check for existing spectroscopic data of required quality ($R \gtrsim 40\,000$ and $S/N \sim 100$) and cadence (minimum two-epochs) in public (including ESO archives).

We were left with a total of 272 stars that we ultimately targeted with the UVES and FEROS instruments. The sample was divided in two parts according to the V -band magnitude of the target. Fainter stars with $V_{\text{mag}} > 10$ were observed with the UVES instrument while brighter objects with $V_{\text{mag}} \leq 10$ were targeted with the FEROS instrument. This strategy allowed us to achieve maximal observing efficiency. In particular, this implied

² <https://www.eso.org/public/teles-instr/paranal-observatory/vlt/vlt-instr/uves/>

³ <https://www.eso.org/public/teles-instr/lasilla/mpg22/feros/>

⁴ <http://simbad.u-strasbg.fr/simbad/>

that none of the UVES science exposure were dominated by the instrument's system overhead.

The choice to take two-epoch spectroscopic observations was driven by the need to (i) uncover potential binaries in our sample, and (ii) detect possible variations in spectral lines (He, Si, Mg, etc.) due to large macroturbulent velocity fields. High values of macroturbulence were previously reported for many high-mass stars (e.g., Simón-Díaz & Herrero 2014; Simón-Díaz et al. 2017). Moreover, a link between the physics underlying this phenomenon and non-radial gravity modes and/or IGWs has been suggested (Aerts & Rogers 2015; Bowman et al. 2020). To avoid misinterpretation of detected variability due to strong tidal interactions between two stars in a (close) binary system rather than being intrinsic, uncovering such systems is of great importance. The two spectroscopic observations per object have been separated by at least 2-3 weeks to ensure detection capability for both short- and intermediate-period binaries where tidal forces are expected to be strongest.

2.6. Further content and goals of this paper

As of now, we focus on the global spectroscopic analysis of a sub-part of our overall stellar sample of 272 OB stars in the Galaxy and LMC. In particular, we perform the analysis of the entire UVES sample of 105 stars, composed of mostly blue supergiants in the LMC and a few dwarfs in the Milky Way. We extend this sub-sample with 43 LMC blue supergiant stars observed with the FEROS instrument, bringing the total of treated stars in this paper to 148. The remaining 124 galactic objects (98 single stars and 26 spectroscopic binaries) in the FEROS sample are analysed and presented in the accompanying paper by Gebruers et al. (2022).

Our goal for the 148 OB stars (of which 24 are duplicates that are stars observed with both instruments) treated here is twofold: (i) perform a check for binarity and derive stellar atmospheric parameters such as the effective temperature T_{eff} , surface gravity $\log g$, and projected rotational velocity $v \sin i$ and (ii) should the data quality allow for it, investigate the effect of macroturbulent broadening on spectral lines across the sample and its possible connection with stellar oscillations. In the final section, we reconsider the TESS variability classification of the stars according to their spectroscopic parameters.

3. Custom spectroscopic data reduction

The power of asteroseismology for probing the effects of mixing in the radiative envelopes and atomic diffusion in intermediate-to high-mass stars is greatly increased when high-precision inference of atmospheric chemical composition is available for these stars (for example, Mombarg et al. 2022). The required high precision in the determination of atmospheric parameters and chemical composition of stars can only be achieved when the raw spectra are extracted and normalised to the local continuum in an optimal way. As mentioned in Sect. 2, a sub-sample of 124 Galactic objects from our program targeted with the FEROS instrument are analysed in the accompanying paper by Gebruers et al. (2022), where a modified version of the CERES data reduction pipeline⁵ (Brahm et al. 2017) was used to achieve the required precision in the processed spectra.

In this work, we employ the EsoREFLEX data reduction pipeline⁶ (Freudling et al. 2013) to process the data obtained

with the UVES instrument. The data reduction steps include bias subtraction, flat fielding, wavelength calibration, order merging, and removal of cosmic hits. Figures 1(a) and 2(a) show the extracted, wavelength-calibrated, order-merged UVES spectra of an example main-sequence star, HD 41297, and an example blue supergiant, HD 270123, respectively. Both spectra contain a prominent wave-like pattern reminiscent of the individual échelle orders, and this pattern is detected in the reduced spectra of most of our targets. The pattern cannot be properly accounted for during the normalisation process and strongly affects the end results, especially in the wavelength regions of broad hydrogen lines in the spectra of main-sequence stars.

Given that the inferior quality of the spectrum extraction and normalisation is in direct conflict with our needs for future high-precision asteroseismic modelling, we opt to develop a custom reduction pipeline instead. We start with an intermediate product of the ESO pipeline in the form of the blaze-corrected, non-merged échelle orders. These non-merged spectra are subjected to normalisation to the local continuum where we consider the following two approaches: (i) an ‘order-by-order’ method where each individual échelle order is normalised independently by fitting a low-degree polynomial to it (dubbed ‘method 1’), and (ii) a ‘2D method’ where all 30 échelle orders in the blue arm are considered as an ensemble and approximated by a 2D surface of cubic smoothing splines (dubbed ‘method 2’). The individual normalised orders are ultimately merged together with the flux being represented by the weighted mean in the overlapping regions of the consecutive orders. The weights are assumed to be increasing with the distance from the edge of the order such that the order edges characterised by high levels of noise have negligible contribution to the mean flux value.

We find that both of these two new methods give comparable results. Typical examples of the normalised spectra are shown in Figs. 1(b,c) and 2(b,c) for a galactic main-sequence star with broad hydrogen lines and a blue supergiant in the LMC, respectively. One can see that, in the case of blue supergiants that do not display broad hydrogen lines spanning the whole échelle order or beyond (cf. Fig. 2(c)), a simple order-by-order-based method leads to normalised spectra of high quality. In particular, these spectra are free of the pattern reminiscent of the individual échelle orders that is otherwise present when the normalisation is performed on the order-merged spectra delivered by the ESO data reduction pipeline.

In the case of main-sequence stars whose broad hydrogen lines often span the whole or even extend beyond a single échelle order, neither of the above-described normalisation methods delivers satisfactory results. We find that the outer wings of hydrogen lines appear to be most affected by the normalisation process (cf. Fig. 1(c)) which in turn leads to erroneous inference of T_{eff} and $\log g$ of the star. In the accompanying paper by Gebruers et al. (2022), a method that assumes simultaneous optimisation of stellar atmospheric parameters and properties of the normalisation function is discussed and employed for the analysis of B- and A-type main-sequence stars. Here, we follow a similar approach. The general idea is to use information on the local continuum placement from a grid of synthetic spectra that spans the parameter range of O- and B-type stars. We employ the Grid Search in Stellar Parameters (GSSP; Tkachenko 2015) software package⁷ to compute a grid of synthetic spectra in the region of the parameter space corresponding to late B-type stars, while O- and early B-type stars are represented by the OSTAR2002 (Lanz

⁵ <https://github.com/rabrahm/ceres>

⁶ <https://www.eso.org/sci/software/pipelines/>

⁷ <https://fys.kuleuven.be/ster/meetings/binary-2015/gssp-software-package>

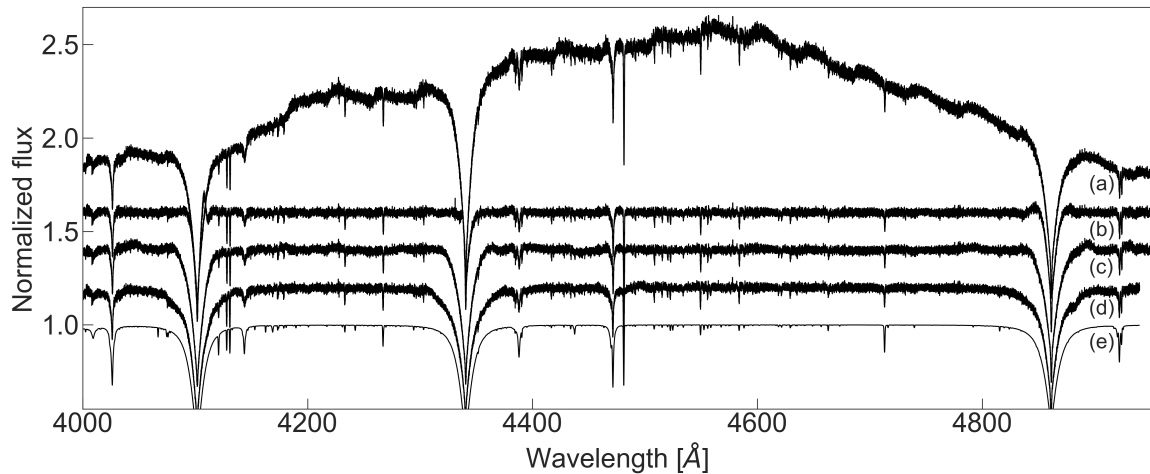


Fig. 1. The uvess spectrum of galactic main-sequence star HD 41297. Panel (a) shows the order-merged non-normalised spectrum extracted with the ESO data reduction pipeline. Panels (b), (c), and (d) demonstrate the spectra normalised by fitting a low-degree polynomial to the individual échelle orders, fitting a 2D smoothing spline to all 30 échelle orders in the uvess blue arm, and iterative fitting of synthetic spectra, respectively. The best fit synthetic spectrum obtained for this star is shown in panel (e) for comparison. See text for details.

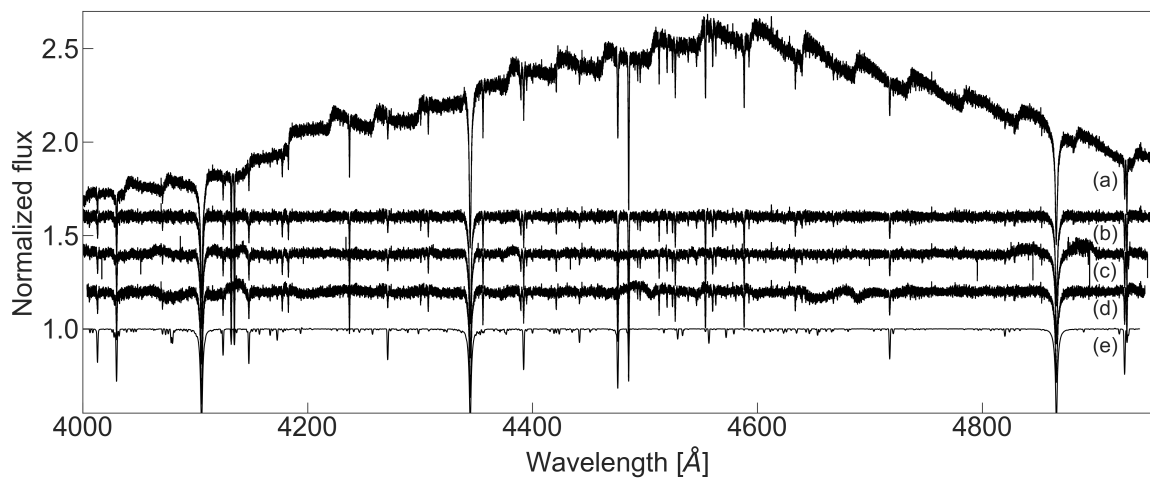


Fig. 2. Same as Fig. 1 but for the uvess spectrum of supergiant HD 270123. See text for details.

& Hubeny 2003) and BSTAR2006 (Lanz & Hubeny 2007) TLUSTY grids.

The normalisation procedure (dubbed ‘method 3’) consists of the following steps: (i) the blaze-corrected non-merged observed uvess spectrum is taken as input and all individual échelle orders are normalised by dividing with low-degree ($n = 3$) Chebyshev polynomial functions; (ii) the coefficients of the individual Chebyshev polynomials are optimised by minimising the difference between the normalised échelle order and synthetic spectrum in the wavelength range covered by that order; (iii) all individual normalised échelle orders are ultimately merged together in a weighted scheme similar to the one described above; and (iv) the best fit synthetic spectrum and normalisation function are obtained by minimising the χ^2 merit function across the entire grid of synthetic spectra in the wavelength range between 4000 and 5000 Å. Figure 1(d) shows the spectrum of an example main-sequence star, HD 41297, normalised using the procedure described above. The difference in quality of normalisation with respect to all other methods considered in this work is most

noticeable around the Balmer lines though small-scale improvements in normalisation are also seen throughout the entire wavelength interval.

For completeness, we apply ‘method 3’ of normalisation to the spectrum of blue supergiant stars. As can be seen in the typical example in Fig. 2(d), there is no improvement in the quality of normalisation compared to the less complex recipe of the order-by-order normalisation method. On the contrary, the quality gets worse in wavelength regions associated with the edges of those échelle orders that are rich with rather narrow absorption features. Therefore, in the rest of this work, we adopt the ‘method 1’ spectrum normalisation for all blue supergiants in our sample.

In order to validate ‘method 3’ of spectrum normalisation, we pick two main-sequence stars, HD 41297 and HD 45527, that were also observed with the FEROS instrument and analysed in Gebruers et al. (2022). In the latter study, the FEROS spectra were processed with the modified version of the CERES data reduction pipeline and subsequently analysed with the ZETA-PAYNE

method (Straumit et al. 2022). The ZETA-PAYNE method employs a pre-trained neural network to predict normalised synthetic spectrum for an arbitrary set of stellar labels such as T_{eff} , $\log g$, $v \sin i$, and [M/H] (and optionally microturbulence ξ). The normalisation function is represented by a series of Chebyshev polynomials and is optimised in the method along with the above-mentioned atmospheric parameters of the star. Application of our ‘method 3’ for normalisation to the UVES spectra of HD 41297 and HD 45527 delivers atmospheric parameters that are consistent within the 1σ confidence interval with those reported in Gebruers et al. (2022).

Finally, we quantify the effect of spectrum normalisation on the inferred atmospheric parameters of three main-sequence stars and three blue supergiants. In this exercise, we consider three different approaches for spectrum normalisation: (i) fitting and dividing the blaze-corrected order-merged observed spectrum (c.f. Figs 1(a) and 2(a)) with a low-degree polynomial (that is the procedure commonly used in the literature); (ii) our ‘method 1’; and (iii) our ‘method 3’. All three methods deliver atmospheric parameters for the blue supergiants that are consistent within the 1σ confidence interval. For the main-sequence stars, however, we find that our ‘method 3’ provides a substantially better representation of the observed spectrum by the best fit model and delivers T_{eff} and $\log g$ that differ by some 1 000 K and 0.9 dex, respectively, from the parameters inferred with the other two methods. Therefore, in the rest of this work, we adopt ‘method 3’ for the spectrum normalisation of all main-sequence stars in our sample according to initial classification of targets’ type (see section 4 for details on classification).

4. Analysis of the UVES and FEROS spectroscopy

In order to provide an empirical estimate for the effective temperature and luminosity of the star and to inform the above-described normalisation process, we first perform an initial classification of all the spectra in our sample. The classification is done by means of visual comparison of the selected spectral line intensities and their ratios to the digital spectral classification atlas of Gray⁸ (Gray & Corbally 2009). We use the pair of Mg II 4481 Å and He I 4471 Å spectral lines as a main diagnostic to assign a spectral type to all stars in the sample. Luminosity classes were decided upon from the strengths of spectral lines of Si, N, O and Fe, depending on the T_{eff} regime: (i) Si IV 4116 Å to He I 4121 Å and N III 4379 Å to He I 4387 Å line strength ratios for late O-type stars; (ii) O II 4070 Å, 4348 Å, 4416 Å and Si III 4553 Å spectral line strengths for early B-type stars; and (iii) line strength of the Si II 4128/4130 Å doublet for late B-type stars. In this way, we identify 5, 49, and 63 stars of late O-, early-B, and late-B spectral classes, respectively. Moreover, not unexpectedly, we confirm our sample to be dominated with evolved blue supergiants (see Table A.1).

4.1. Identification of line profile variations and binary candidates

The strategy of multi-epoch spectroscopic observations allows us to check all our targets for possible binary nature and for particularly strong line profile variations (LPV) due to intrinsic variability of the star. Both of these phenomena are readily revealed in the analysis of radial velocity (RV) variations that occur due to either global line shifts in the spectra of spectroscopic binaries or

line distortions (asymmetries, skewness, etc.) due to variability intrinsic to the star (abundance spots, pulsations, etc.).

We employ the Least-Squares Deconvolution (LSD; Donati et al. 1997) method as implemented in Tkachenko et al. (2013) to compute high S/N average profiles from the absorption lines for all our targets. These average profiles are subsequently analysed to deduce RV values by fitting them with an asymmetric Gaussian profile of the following form:

$$A(x, x_0, \sigma, r) = \frac{1}{\sqrt{\pi\sigma^2(r+1)}} \begin{cases} \exp \left\{ -\frac{(x-x_0)^2}{2\sigma^2} \right\} & \text{if } x > x_0, \\ \exp \left\{ -\frac{(x-x_0)^2}{2r^2\sigma^2} \right\} & \text{otherwise.} \end{cases} \quad (1)$$

Here r is the asymmetry coefficient, σ controls the width of the profile, and x_0 represents the position of the minimum of the profile.

Spectroscopic classification of a star that presumably shows line profile variations due to its intrinsic variability requires a joint interpretation of the inferred RV and coefficient of asymmetry (c.f. Aerts et al. 1999; De Cat & Aerts 2002; Telting et al. 2006). We classify a star as a spectroscopic binary (dubbed either SB1 or SB2 in Table A.1 for the case of single- and double-lined binary, respectively) when (i) the RV difference between the two epochs is larger than 3σ , or (ii) either a global shift of spectral lines and/or double-lined nature are confirmed visually. We take a conservative 3σ interval to account for the fact that the obtained uncertainties are purely statistical resulting from the least-squares fitting method. They are hence an underestimation ignoring any systematic uncertainties. The same two criteria, that is visual inspection and a relative RV difference below 3σ , are used to classify a star as “LPV” in Table A.1, where the visual inspection focuses on LPV in the form of (local) spectral line distortions instead of global shifts. Furthermore, stars that show large global asymmetries in their observed line profiles are put into a separate class, dubbed “asymm” in Table A.1. Ultimately, stars that do not show significant RV variability nor appreciable line asymmetries in the two observed epochs are classified as apparently constant (dubbed “const” in Table A.1). Ambiguous classifications are supplemented with “?”. The results of our classification are summarised in Table A.1 (column designated “variability”).

We stress that no distinction is made at this stage between intrinsic variability of the star originating from pulsations, rotational modulation, or any other physical mechanism, due to the limited amount of information (only two spectroscopic epochs) and simplicity of the employed classification method. Figure 3 shows examples of the observed LSD profiles with the best fit asymmetric Gaussian profile models overlaid for SK -70 77 (top left), HD 268729 (top right), SOI 404 (bottom left), and HD 268654 (bottom right), which represent typical behaviour for different variability groups. These stars are classified as apparently constant (“const”), spectroscopic binary candidate (“SB1”), line profile variable (“LPV”), and one showing appreciable line asymmetries (“asymm”), respectively.

In this way we identify 65 (21), 6 (1), 15 (13), and 22 (15) apparently constant stars, stars with LPV, spectroscopic binary candidates, and stars with appreciable line asymmetries, respectively, in the UVES (FEROS) sample. Of those detections, 0 (0), 3 (1), 12 (11), and 9 (12) are tentative classifications meaning that more observational epochs are required to draw definitive conclusions as to the exact type of spectroscopic variability.

⁸ <https://ned.ipac.caltech.edu/level5/Gray/frames.html>

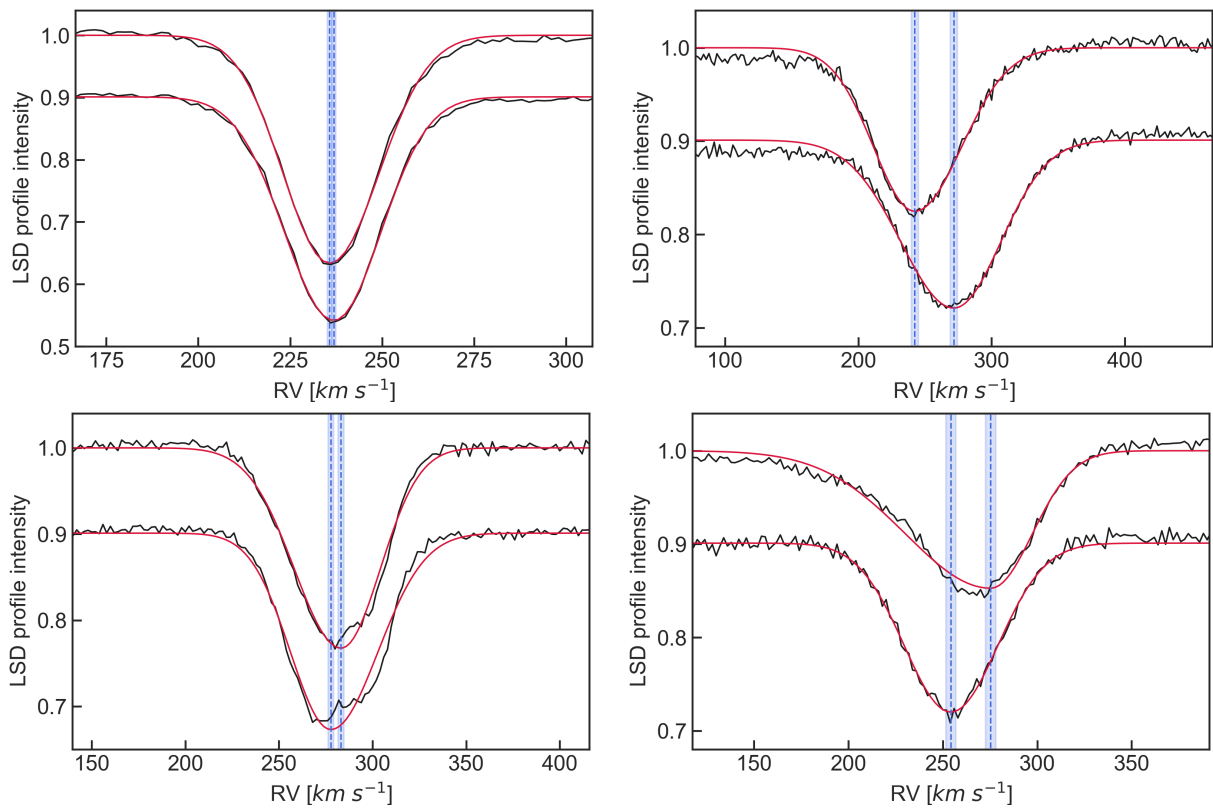


Fig. 3. Comparison of the observed LSD profiles with the best fit asymmetric Gaussian profile models. From top left to bottom right: SK -70 77, HD 268729, SOI 404, and HD 268654 (all were classified as blue supergiants). Blue lines indicate the inferred RVs while the shaded areas reflect the corresponding 1σ uncertainty intervals.

4.2. Inference of the projected rotational velocity $v \sin i$

Measuring the projected rotational velocity $v \sin i$ from the spectrum of an early-type star is not a straightforward task. Lines are typically broadened by several physical mechanisms acting simultaneously in the atmospheres of these stars, ultimately leading to an appreciable overestimation of the $v \sin i$ parameter when other mechanisms are ignored in the analysis. Simón-Díaz & Herrero (2014) and Simón-Díaz et al. (2017) stress that the contribution of a macroturbulent velocity, Θ , to the total broadening of spectral lines in O- and B-type stars can be as large as the contribution associated with $v \sin i$, and in many cases even exceed it. Aerts et al. (2014) demonstrate that the macroturbulent and projected rotational velocities cannot be reliably inferred from single snapshot spectroscopic observations of intrinsically variable (spotted and/or pulsating) early-type stars whose spectral lines show pronounced LPV. In particular, the authors stress that $v \sin i$ and Θ vary appreciably and in anti-phase with each other during the pulsation cycle, where Θ can vary by as much as a few tens of km s^{-1} during the pulsation cycles.

Cantiello et al. (2009) report a strong anti-correlation between the microturbulent velocity ξ and surface gravity $\log g$ in the LMC sample of B-type stars analysed in Hunter et al. (2008). The authors suggest a connection between microturbulence and velocity fields triggered by gravity waves induced in the iron sub-surface convection zone. It is also worth mentioning that the most evolved among B-type stars studied in Hunter et al. (2008) show microturbulence as large as some 20 km s^{-1} which is in line with Gray (2008, Chapter 17) who also suggests vertical stratification of microturbulence in photospheres of evolved hot stars. In summary, the total line broadening observed in spectra of intermediate- to high-mass stars is typically

a combination of several line broadening mechanisms such as stellar rotation, micro- and macroturbulence, and stellar oscillations. In the most extreme cases, all of these mechanisms will have comparable magnitudes which unavoidably leads to strong degeneracy between the corresponding parametric descriptions in the modelling of individual spectral lines or their ensembles.

In order to provide as reliable estimate of $v \sin i$ as possible for all stars in our sample, we employ a method that is based on the Fourier transform (FT) of a spectral line profile (Carroll 1933; Gray 2008, Chapter 2). This method relies on the fact that the FT of a rotationally broadened profile consists of multiple lobes separated by zeros (see the right panel of Fig. 4). The position of the first zero and the associated frequency in the FT translates directly into the projected rotational velocity $v \sin i$ of the star (denoted as $v \sin i_{\text{FT}}$), provided that the dominant line broadening contribution delivers a time-independent profile (see Eq. (1) in Simón-Díaz & Herrero 2014). An application is shown in the left panel of Fig. 4. A convolution of the rotational profile with profiles due to other broadening mechanisms transforms into multiplication in Fourier space, which preserves the positions of the zeros. Therefore, identification of the first zero in the FT allows us to isolate the effect of $v \sin i$ from other broadening mechanisms affecting the line profile, provided that: (i) additional line broadening mechanisms can be represented by a convolution, that is they are independent of each other; and (ii) these mechanisms do not share the same frequency regime with rotational broadening. Such conditions are typically not satisfied when $v \sin i \lesssim 50 \text{ km s}^{-1}$ and/or when time-dependent phenomena are dominant in the line-forming region (Aerts et al. 2014). Note that the FT method also becomes less reliable if the macrotur-

bulent velocity parameter Θ exceeds $v \sin i$ as lobes and zeroes smear out, as shown in the right panel of Fig. 4.

The position of the first zero in the FT of the line profile is also affected by the limb darkening effect. Following Claret & Bloemen (2011), the linear limb darkening coefficient ϵ is found to be around 0.35 in the case of B-type stars, which is significantly lower than the value of $\epsilon = 0.6$ often used as reference in studies of solar-type stars. The uncertainty in ϵ leads to a noticeable shift of the first zero in the FT of the line profile (see the middle panel of Fig. 4) which translates into a small yet systematic difference of up to 10 % in the inferred value of $v \sin i$. Therefore, we fix $\epsilon = 0.35$ for the determination of $v \sin i_{\text{FT}}$ and neglect any small object-to-object variations of the coefficient within the sample.

Because the FT method is most suitable for isolated and undistorted line profiles, a careful selection of the latter is required. We rely on the Si II 4128 Å and Si III 4552 Å lines for the late and early B-type stars in our sample, respectively. The Mg II 4481 Å line is used in all other cases unless its visual inspection reveals either poor quality in terms of S/N or a high degree of asymmetry. In those cases, we choose He I 4471 Å as an alternative, even though helium lines are generally not the best choice because of their large intrinsic pressure-dominated broadening. However, because of a general lack of metal lines in the spectra of hot stars and our sample being dominated by blue supergiants characterised by low $\log g$ values, the He I 4471 Å line is a reasonable alternative in the absence of isolated undistorted metal lines. Furthermore, given that LPV due to stellar pulsations may lead to appreciable variations in $v \sin i_{\text{FT}}$ for each star (Aerts et al. 2014), we infer the stellar projected rotational velocities from individual epoch spectra instead of their co-added version. The finally accepted value of $v \sin i_{\text{FT}}$ is the average between the two epochs of observations while its temporal variability (if detected) is interpreted as systematic uncertainty due to temporal variability of the line profiles. The respective $v \sin i$ values and their uncertainties are reported in Table B.1 (column designated $v \sin i_{\text{FT}}$).

Another commonly used method to infer $v \sin i$ is through fitting either individual line profiles or the entire spectrum of the star by a set of synthetic models. As discussed above, we expect this method to lead to an over-estimation of $v \sin i$ if other broadening mechanisms are ignored in the fitting procedure while they may contribute to the total line broadening, as is often the case in the spectra of early-type stars. To quantify the effect, we estimate $v \sin i$ for all stars in the sample by performing the fit to the full spectra with synthetic models and by assuming no macroturbulent velocity. The respective parameter values are reported in Table B.1 and are compared to the $v \sin i$ values inferred with the FT method in Fig. 5 (right panel). One can see that the $v \sin i$ values inferred from the method of synthetic spectra are up to 30 % higher compared to those inferred with the FT method. Indeed, the former method gives an indication of the total broadening when other broadening mechanisms are not directly included in the fitting, while the latter method to a large extent treats the rotational broadening separately from the other mechanisms.

4.3. Inference of the effective temperature T_{eff} and surface gravity $\log g$ of the sample stars

As mentioned in Sect. 3, we rely on three grids of synthetic spectra for our analyses. We fit the normalised observed spectra with those predicted by models in the grids by means of a χ^2 -minimisation to find the best-fit parameters. The fitting is

performed in the wavelength range of 4000–5000 Å, which includes a plethora of metal and helium lines, as well as the H_β , H_γ , and H_δ lines. The minimisation is performed with the Trust Region Reflective algorithm (Conn et al. 2000) applied to the $T_{\text{eff}} - \log g - v \sin i$ parameter space, where the model spectra for the parameter values are interpolated from those in the grids at each step of the iteration. The ostar2002 (Lanz & Hubeny 2003) and bstar2006 (Lanz & Hubeny 2007) grids of TLUSTY models are employed for the analysis of a few predominantly upper main-sequence stars in the sample. Furthermore, owing to the fact that our sample is dominated by evolved blue supergiants in the LMC with $T_{\text{eff}} \gtrsim 10\,000$ K and that the ostar2002 and bstar2006 grids do not extend towards low $\log g$ values characteristic for supergiant stars, we compute a dedicated grid of CMFGEN (Hillier & Miller 1998) models covering $\log g$ values as low as 1.7 dex. The parameter space of the grid is dictated by the lowest $\log g$ possible for a given T_{eff} such that the star remains in hydrostatic equilibrium. This way, the grid extends from 11 000 K to 19 000 K in T_{eff} while $\log g$ ranges from 1.7–2.5 dex at 11 000 K and from 2.2–2.5 dex at 19 000 K. Owing to the large computation time, a step of 1 000 K and 0.1 dex is chosen for T_{eff} and $\log g$, respectively. The parameter space covered with the CMFGEN grid is indicated with the grey shaded area in Fig. 6.

A grid of the LTE-based GSSP (Tkachenko 2015) models is used for the analysis of a few unevolved stars with $T_{\text{eff}} \lesssim 15\,000$ K, a range in the parameter space not covered by the bstar grid of the TLUSTY models and where the use of CMFGEN is not justified. The GSSP grid is designed such as to cover a T_{eff} range between 9 000 K and 15 000 K. By analogy with the CMFGEN grid and for exactly the same reason (i.e. the star needs to remain in the hydrostatic equilibrium), the $\log g$ range is set to 2.5–4.5 dex for $T_{\text{eff}} < 10\,000$ K and to 3.0–4.5 dex for $T_{\text{eff}} \gtrsim 10\,000$ K. The step in T_{eff} is 100 K and 250 K for $T_{\text{eff}} < 10\,000$ K and $T_{\text{eff}} > 10\,000$ K, respectively, while the step in $\log g$ is fixed to 0.1 dex. We assume the solar chemical composition as derived in Grevesse et al. (2007). This way, we adopt adequate tools for each of the three regimes of stars in our sample. The regions of the parameter space covered by the grids of GSSP, TLUSTY, and CMFGEN models used in this study are illustrated with shaded areas in Fig. 6.

Spectroscopic inference of surface abundances for the sample stars is the subject of a follow-up paper. For this reason, we fix the microturbulent velocity ξ to 2 km s⁻¹ and 10 km s⁻¹ for all unevolved (GSSP and TLUSTY) and blue supergiant (CMFGEN) models, respectively. Furthermore, we assume solar and about half solar ([M/H]=−0.4 dex) metallicity for all the Galactic and LMC (Choudhury et al. 2021) targets, respectively. The results of the spectroscopic analysis based on this approach are summarised in Table A.1, where the grid of used atmosphere models for a particular target is indicated with the superscript “a”, “b”, and “c” for GSSP, TLUSTY, and CMFGEN, respectively. The positions of the stars in the spectroscopic $\log T_{\text{eff}} - \log(T_{\text{eff}}^4/g)$ HR diagram are shown in Fig. 6. The $v \sin i$ values inferred from this fitting approach (representing the total line broadening) are also provided in Table B.1. As it was suggested in Sect. 3 already, the majority of the sample stars are found to be blue supergiants, with just a few objects in their main-sequence stage of evolution. We find four objects that have masses in the range between some 2.5 and 4.0 M_⊙, with three of them being located within the SPB instability region while the fourth object is found at the border when uncertainties are taken into account. The rest of the stellar sample is consistent with masses in excess of 10 M_⊙.

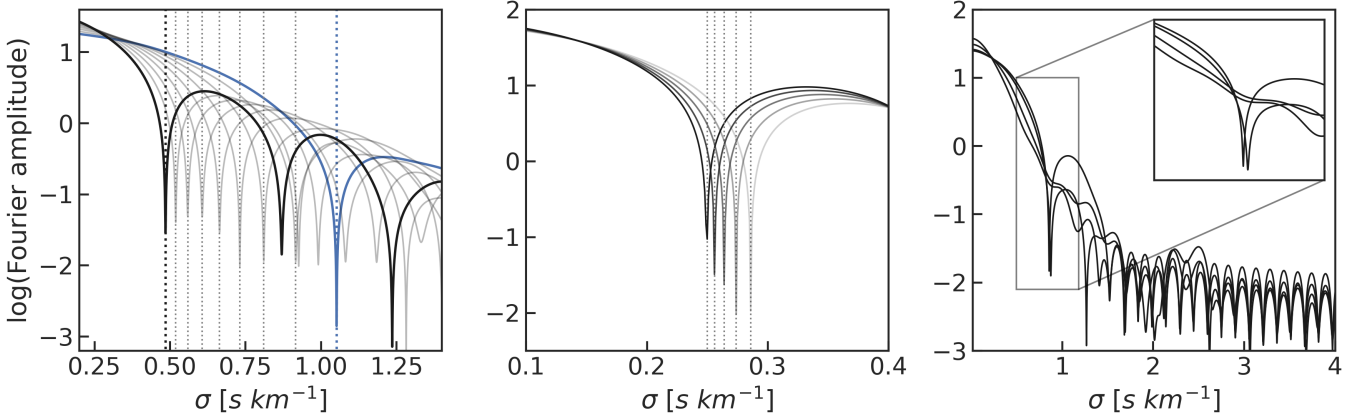


Fig. 4. Fourier transforms of synthetic line profiles with positions of the first zero indicated with vertical dotted lines. Left panel: the $v \sin i$ parameter is varied from 42 km s^{-1} (blue) to 90 km s^{-1} (black) with a step of 6 km s^{-1} (grey). Middle panel: the linear limb darkening coefficient ϵ is varied from 0.2 (black) to 1.0 (light grey), while $v \sin i$ is kept fixed at 50 km s^{-1} . Right panel: a different contribution of the macroturbulence Θ to the total line broadening is assumed: $\Theta/v \sin i = 0.3, 0.6, 1.2$ and 1.8 , with $v \sin i$ fixed to 50 km s^{-1} . The inset is a close up into the region of the position of the first zero.

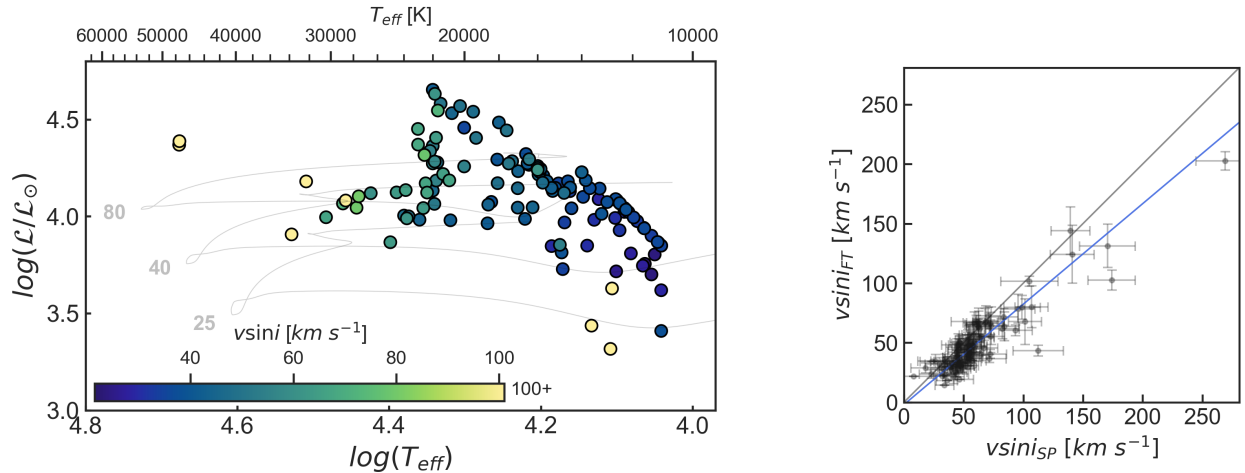


Fig. 5. Results of $v \sin i$ inferences. Left panel: positions of the sample stars in the spectroscopic HR diagram. Individual objects are colour-coded by their $v \sin i$ value inferred from the Fourier method. Right panel: comparison of $v \sin i_{\text{SP}}$ with $v \sin i_{\text{FT}}$. The grey line shows the case where $v \sin i_{\text{FT}}$ and $v \sin i_{\text{SP}}$ are equal, while the blue line is an error-weighted fit to the observed values.

4.4. Inference of the macroturbulent velocity

As discussed in Sect. 4.2, massive stars are known to show macroturbulent velocity fields that are often comparable to or exceed the spectral line broadening associated with the stellar rotation (e.g., Aerts et al. 2014; Simón-Díaz & Herrero 2014; Simón-Díaz et al. 2017). There is currently no consensus achieved as to the exact physical mechanism(s) responsible for the macroturbulent broadening in the spectral lines of massive stars. Two main hypotheses are (i) the collective effect of gravity waves, either heat-driven (Aerts et al. 2009) or stochastically excited at the boundary between the convective core and radiative envelope in these stars (Aerts & Rogers 2015); and (ii) velocity perturbations due to turbulent pressure in the subsurface convection zone driven by the iron opacity peak at some 150 kK (Cantiello et al. 2021). These two hypotheses are not mutually exclusive (Bowman et al. 2020; Bowman & Dorn-Wallenstein 2022).

Our stellar sample is well suited to infer the macroturbulent velocity Θ , as well as to estimate the relative contributions of

its radial Θ_R and tangential Θ_T components. Indeed, we were able to acquire high-resolution, high S/N, multi-epoch spectroscopic data for the majority of objects in the sample. Furthermore, the sample is composed of stars spanning a wide range of stellar mass ($M \in [3, 80] M_\odot$) and spectroscopic luminosity ($\log(\mathcal{L}/\mathcal{L}_\odot) \in [1.8, 4.5]$, cf. Fig. 6). Therefore, we proceed with the observational characterisation of the macroturbulent velocity field using synthetic spectra to fit $\text{Mg II } 4481 \text{ \AA}$ line profiles. Macroturbulence is treated with a radial-tangential prescription as defined in Takeda & Ueno (2017) for an area element, where a locally broadened profile is defined by a convolution of an intrinsic profile and a macroturbulent kernel:

$$I(v, \theta) = I^0(v, \theta) * K(v, \theta). \quad (2)$$

Here, v stands for the profile velocity from transforming the wavelength with respect to the central wavelength of the line, while θ defines a direction angle into the observer's line-of-sight. The quantity $K(v, \theta)$ is the convolution kernel due to the macro-

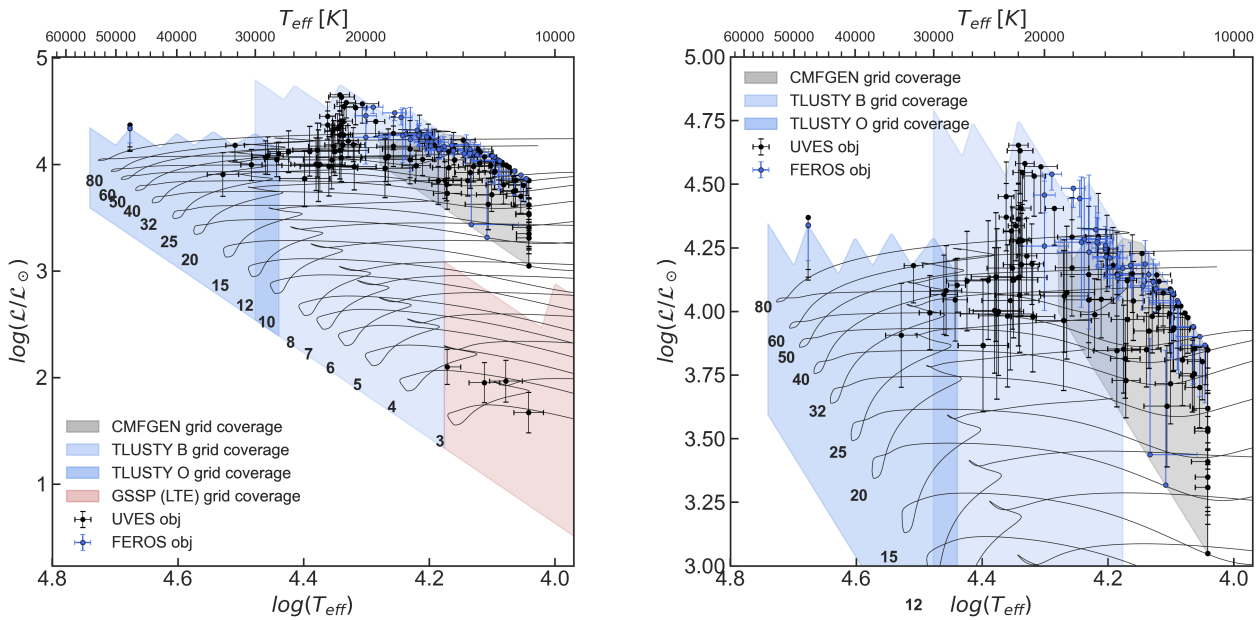


Fig. 6. Positions of the sample stars in the spectroscopic $\log(T_{\text{eff}})$ - $\log(L/L_{\odot})$ HR diagram. The UVES and FEROS samples are shown with black and blue symbols with error bars, respectively. Regions of the parameter space covered by the GSSP, TLUSTY, and CMFGEN models are marked with red, blue, and grey shaded areas, respectively. Nonrotating MESA stellar evolution tracks computed for $Z = 0.006$ are shown with black solid lines and are taken from Burssens et al. (2020). Left panel: full parameter range. Right panel: zoom into the high-luminosity region where the bulk of the sample is situated.

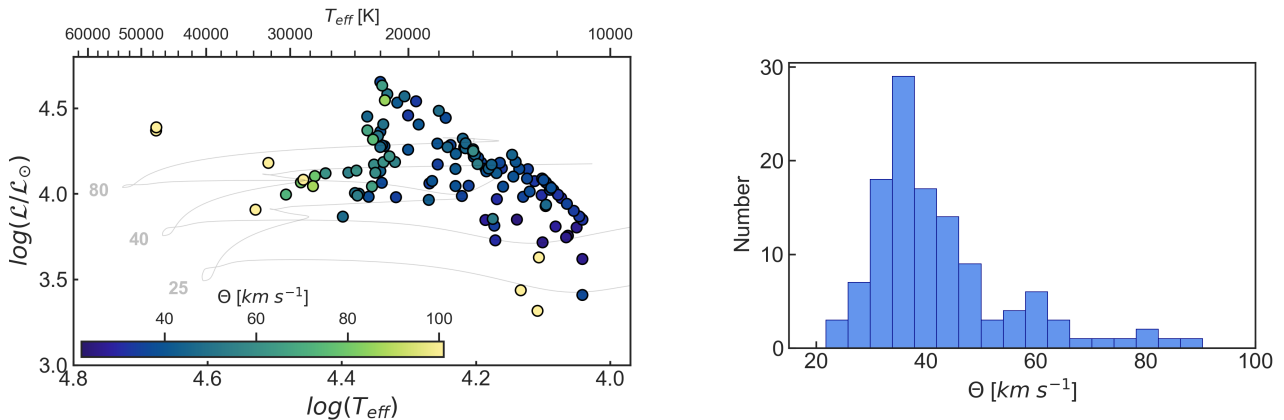


Fig. 7. Results of the inference of the macroturbulence parameter Θ . Left panel: stellar positions in the spectroscopic HR diagram colour coded by the inferred value of the macroturbulent velocity parameter Θ . Value of the macroturbulent velocity is an error-weighted of two epochs. Right panel: distribution of the macroturbulent velocity parameter Θ across the sample.

turbulent broadening and is defined as:

$$K(v, \theta) = \frac{a_R}{\pi^{1/2} \Theta_R \cos \theta} \exp \left[-\frac{v^2}{(\Theta_R \cos \theta)^2} \right] + \frac{a_T}{\pi^{1/2} \Theta_T \sin \theta} \exp \left[-\frac{v^2}{(\Theta_T \sin \theta)^2} \right]. \quad (3)$$

The most common approach in the literature to estimate macroturbulence is the one assuming isotropy, that is $a_R = a_T = 0.5$ and $\Theta_R = \Theta_T = \Theta$.

After convolving the local specific intensities $I^0(v, \theta)$ with the kernel $K(v, \theta)$, the final broadened profile is computed by integrating synthetic specific intensities $I(\mu = \cos \theta)$ based on

our deduced T_{eff} and $\log g$ over the visible sphere for all individual targets. This way, the limb darkening effect is included directly as opposed to the less detailed yet commonly used approach in the literature relying on parametric approximations. In our method, we make the following assumptions: (i) similar to the case of the parameter inference for $v \sin i$, T_{eff} , and $\log g$ (cf. Sects 4.2 and 4.3), we fix the value of the microturbulent velocity to 2 km s^{-1} and 10 km s^{-1} for all main-sequence and supergiant stars in the sample, respectively; (ii) the $v \sin i$ parameter is varied in the range determined by its value and uncertainties inferred with the Fourier-based method (cf. Sect. 4.2); (iii) in first instance, the macroturbulent parameter Θ is estimated assuming equal contributions of its radial and tangential components (i.e.

the isotropic case); and (iv) because specific intensities are not available for the CMFGEN and TLUSTY models, they are calculated from gssp at the grid node closest to the parameters of the star in consideration. We introduce a line depth correction factor and apply it to the gssp model when fitting the observed profile to account for the difference between the gssp LTE and CMFGEN/TLUSTY non-LTE models. This approach allows us to properly scale the LTE-based intrinsic profile to the expected depth while any possible difference in the shape of the intrinsic profile between the LTE and non-LTE models is considered negligible compared to the total spectral line broadening due to the combined effect of $v \sin i$, ξ , and Θ .

Figure 7 summarises the obtained results in the form of the distribution of stars in the spectroscopic HR diagram colour coded by the inferred value of the macroturbulent velocity (left panel) and a histogram of the estimated values (right panel). In the left panel of Fig. 7, one can see a tendency of increasing macroturbulent parameter as the effective temperature and spectroscopic luminosity of the star increase. A similar trend has been previously reported in Simón-Díaz et al. (2017) (their figure 5) who also concluded that stars in the upper part of the spectroscopic HR diagram ($M \geq 15 M_\odot$) tend to show line profiles with predominantly macroturbulent broadening as opposed to rotational broadening. In the right panel of Fig. 7, one can see that the majority of stars in our sample have a macroturbulent broadening parameter Θ between some 20 km s^{-1} and 70 km s^{-1} , with just a few objects being characterised by Θ below or above that range of values. Correcting for the sample size, which in our case is about four times smaller, and for larger contribution of more evolved objects, the range of the inferred macroturbulent velocity values is consistent with Simón-Díaz et al. (2017). This is a particularly interesting observation given that the stellar sample analysed in Simón-Díaz et al. (2017) is fully comprised of galactic objects while ours is dominated by stars in the LMC, hence representing a substantially different metallicity regime.

As a next step, we attempt to estimate from an observational viewpoint the individual contributions of the radial, Θ_R , and tangential, Θ_T , components of the macroturbulence. In the radial-tangential prescription of macroturbulence, the contribution of the components may be controlled by parameters a_R and a_T such that $a_R + a_T = 1$. The parameter a may be seen as the relative ratio of cells moving tangentially or radially in a unit area. Methodologically, we expand the parameter vector by a_T , where the contribution of the radial component is assumed to be $a_R = 1 - a_T$. The top panel in Fig. 8 shows the results obtained from the fits, relying on an initial value of 0.5 for a_T . The majority of stars tends to show an equal or more dominant tangential component. The middle and bottom panels in Fig. 8 offer a closer look upon the dependence of the obtained results for a_T with respect to its assumed initial value. The distributions (in the form of histograms and Kernel Density Estimations) of a_T are shown for three values of its initial guess, $a_T = 0.25$ (yellow), 0.5 (blue), and 0.75 (green). The main conclusions that can be drawn from these distributions are: (i) the peak position correlates with the initial guess assumed for a_T ; (ii) the peak height decreases in the KDE plot as the initial guess for the a_T parameter decreases; (iii) all distributions are skewed towards higher values of a_T , where the skewness of the observed distribution is statistically significant as confirmed by a Kolmogorov-Smirnov test with respect to a reference Gaussian distribution centered at the peak of the observed distributions; and (iv) visual inspection of observed profiles reveals most of the outlying values ($a_T < 0.4$ and $a_T > 0.8$) to be due to a high level of noise in the spectra and/or strongly asymmetric line profiles. At the same time, spectra of the best

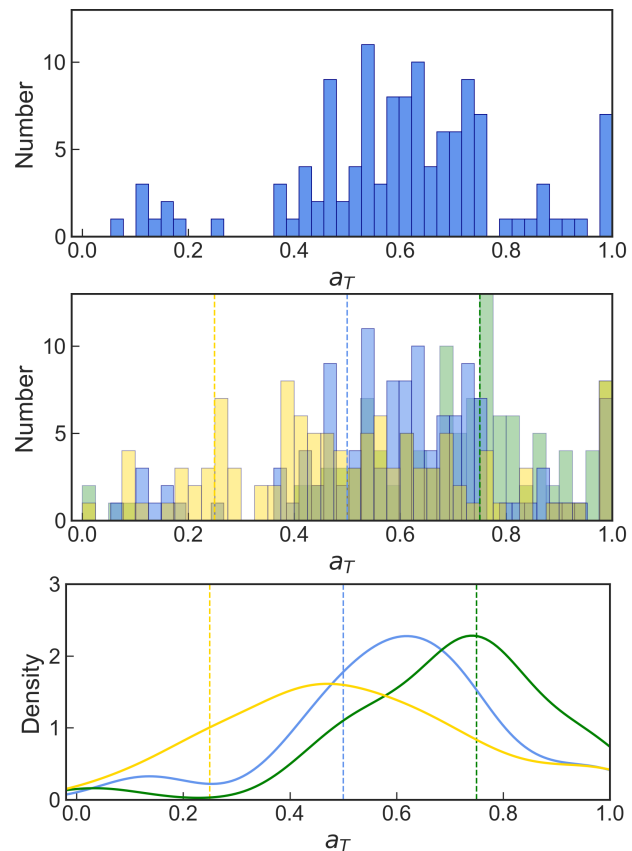


Fig. 8. Results of the inference of the tangential component of macroturbulence. Top panel: histogram of a_T contributions derived from observed profiles of the entire sample with $a_T = 0.5$ as an initial assumption, $v \sin i$ varied within errors of $v \sin i_{\text{FT}}$. Middle panel: histograms of a_T contributions derived from observed profiles of the entire sample with different initial assumptions: 0.25 (yellow), 0.5 (blue), 0.75 (green), $v \sin i$ varied freely. Bottom panel: KDE (kernel density estimate) functions for the same data as in the middle panel. Dashed lines mark initial guesses. The fits demonstrate the results are sensitive to the initial guess.

quality in the entire sample tend to show $a_T/a_R \sim 1$, where the estimated uncertainty of a_T may reach up to 20% for the case treated here.

Furthermore, we compare Θ when $a_T = 0.5$ is fixed and Θ when a_T is included as a free parameter and analyse the trends they demonstrate. The comparison (Fig. 9, left panel) illustrates that these Θ are in agreement to within their uncertainties, while the errors increase significantly when a_T is varied. There is no obvious trend in the distribution of a_T with respect to the value of Θ for $a_T = 0.5$ fixed, as shown in the right panel of Fig. 9.

Finally, following the statistical approach in Aerts et al. (2023), we investigate observed trends in Θ quantitatively from multivariate linear regression models relying on five predictors, of the following form:

$$\Theta = c_0 + c_1 \log(T_{\text{eff}}) + c_2 \log(g) + c_3 \log(\mathcal{L}/\mathcal{L}_\odot) + c_4 v \sin i + c_5 a_T. \quad (4)$$

After consecutive elimination of the insignificant predictors based on the adjusted R^2 -statistics taking into account the degrees-of-freedom, we conclude that the best regression model includes only $v \sin i$ and T_{eff} as relevant predictors, with the following coefficients:

$$\Theta = 66(24) + 17.7(5.8) \log(T_{\text{eff}}) + 1.15(0.02) v \sin i. \quad (5)$$

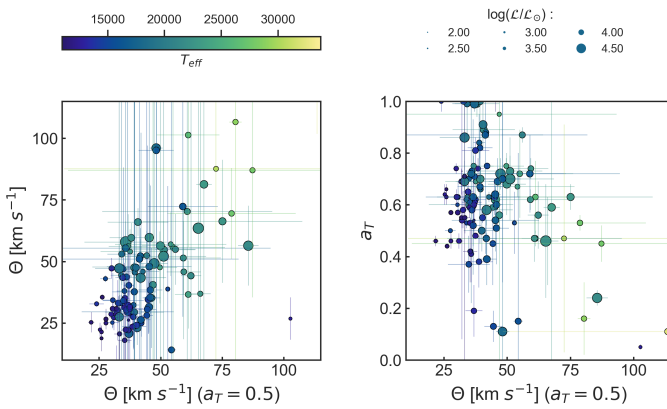


Fig. 9. Results of the inference of the tangential component of macroturbulence. Left panel: comparison of Θ measured with fixed tangential component contribution $a_T = 0.5$ and Θ measured when a_T varied freely. Right panel: distribution of tangential component contribution a_T over Θ . Colour encodes T_{eff} , while symbol size changes with spectroscopic luminosity.

This model explains 96.4% of the observed variability in Θ . We plot the predicted Θ from this regression model together with the observed values for our sample in Fig. 10. There is a clear trend in the $v \sin i$ - Θ plot showing an almost one-to-one correspondence between Θ and $v \sin i$. Our regression results are remarkably similar to those in the recent study by Aerts et al. (2023), who analysed the correspondence between macroturbulent broadening and $v \sin i$ for a large sample of $\sim 15\,000$ galactic gravity-mode pulsators in core-hydrogen burning from low-resolution Gaia DR3 spectra. Moreover, as we mentioned earlier in this section, a similar trend between Θ and $v \sin i$ was found from high-resolution spectroscopy by Simón-Díaz et al. (2017), who analysed a galactic sample of O and B stars. Since our sample consists mostly of LMC objects and thus represents a significantly lower metallicity regime, it is interesting to compare the results for Θ of our stars with those in the sample of Simón-Díaz et al. (2017) to check if there is any dependence on metallicity. We plot the macroturbulent values from Simón-Díaz et al. (2017) and from our work in Fig. 11. Though the Θ values in their sample are in general larger for their supergiants than for ours (note that the first green peak in the right panel corresponds to main-sequence stars, which are absent in the LMC sample), the differences remain roughly within the errors of Θ determined for our sample stars. Since our sample is populated with more luminous stars, and different methods were used to measure Θ , it is difficult to conclude if the shift towards lower Θ in our LMC sample has a physical or methodological origin, also because there are no errors listed for values of the macroturbulent broadening in the study by Simón-Díaz et al. (2017).

5. Improving the inference of macroturbulence

In the above parameterised estimation of the macroturbulent velocity and of its individual radial and tangential component contributions to the line broadening of our sample stars, we made two fundamental assumptions: (i) the microturbulent velocity ξ is known a priori (for example, estimated along with T_{eff} and $\log g$ of the star or fixed to a value typical for a given spectral type and luminosity class), and (ii) the typical $S/N \approx 100$ in the observed spectra is sufficient to distinguish between different line broadening mechanisms. Although these assumptions are motivated by the most commonly used methodologies and/or

Table 1. Combinations of the Θ , ξ , and $v \sin i$ parameter values used in the analysis of spectral line broadening due to the macroturbulent velocity and its interplay with the two other broadening mechanisms. See text for details.

S/N	T_{eff} (K)	$\log g$ (dex)	ξ	Θ (km s $^{-1}$)	$v \sin i$
100, 150, 250	12 000, 22 000	4.0	8	30	15
				30	50
			15	100	15
			65	65	150
100, 150, 250	12 000	4.0	2, 8, 16	30	15

empirical evidences in the literature (e.g. Simón-Díaz et al. 2017; Holgado et al. 2018), they may not be valid. To investigate this, we look into the problem in more detail, attempting to find out (i) what are the requirements in terms of S/N, spectral line selection, etc. for a meaningful inference of the macroturbulent parameter Θ from spectra of O and B stars, (ii) what are the analysis limitations associated with the parameter correlations, in particular between micro- (ξ) and macro- (Θ) turbulent velocities and rotational broadening $v \sin i$, and (iii) under what conditions can one empirically estimate individual contributions of the radial, a_R , and tangential, a_T , components of the global macroturbulent broadening in the spectra of O and B stars.

The above questions are particularly important to address in light of the high sensitivity of the results obtained in Sect. 4.4 to the initial guess of a_T . Moreover, the ability to realistically estimate individual contributions of the radial and tangential components of the macroturbulent broadening is a powerful observational test of various theoretical hypotheses for the origin of macroturbulence as a physical phenomenon. In particular, should wave-driven broadening be at the origin of macroturbulence, one would expect the radial component to dominate over the tangential one in the case of pressure waves, whereas the opposite is true for the case of gravity waves. So far, an appreciable effort has been put in the literature into estimating the macroturbulent velocity parameter Θ for as many massive stars as possible, and to search for possible correlations with various physical mechanisms at work (e.g. Simón-Díaz & Herrero 2014; Simón-Díaz et al. 2017). However, the most common approach is to assume equal contributions of the radial and tangential components, while this choice is the least justified in the case of pulsational broadening (Aerts et al. 2009, 2014).

We simulate synthetic spectra of a late and early B-type star with $T_{\text{eff}}=12\,000$ K, $\log g=4.0$ dex and $T_{\text{eff}}=22\,000$ K, $\log g=4.0$ dex, respectively, to analyze them as they are observed ones and quantify deviations from the true parameters. In the case of the late B-type star, we focus on the Mg II 4481 Å spectral line, while we use the Si III 4552 Å, 4557 Å, and 4574 Å triplet in the early B-type star. Spectra are simulated for several combinations of the parameters Θ , ξ , and $v \sin i$ to consider cases where their dominant role is interchanging. Table 1 provides a summary of all combinations used and we repeat the analysis for three values of $S/N=100$, 150, and 250 to address the influence of the quality of observations on the obtained results. At

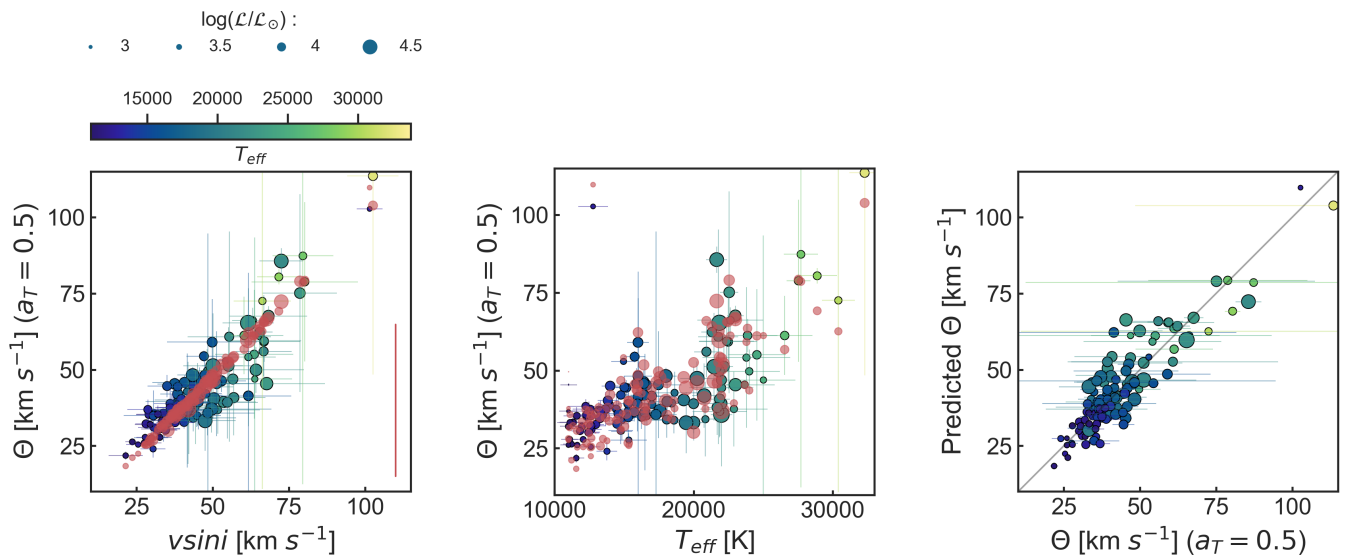


Fig. 10. Results of the multivariate linear regression models for Θ . Left panel: comparison between Θ and $v \sin i$. The colours encode T_{eff} , while the symbol sizes change with spectroscopic luminosity. The red circles show the predicted Θ value from the best multivariate regression model in Eq. (5) for our LMC sample. The red vertical line in the corner indicates a typical error bar for the predicted Θ values and applies to all three panels. Middle panel: comparison between observed Θ and predictor T_{eff} , where Θ predicted from Eq. (5) is colour coded in red. Right panel: comparison of Θ predicted from Eq. (5) and the measured values of Θ .

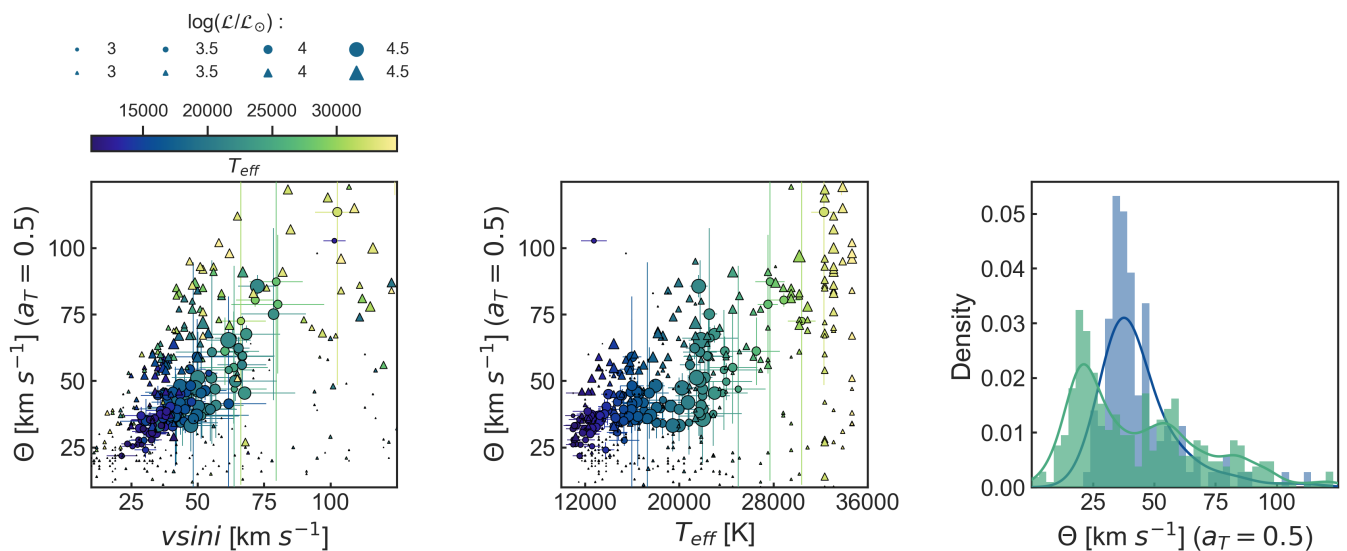


Fig. 11. Comparison of Θ observed in our sample and Θ for the sample treated by Simón-Díaz et al. (2017). Circles show the results for our LMC stars while triangles are the results from Simón-Díaz et al. (2017) for their sample of O and B stars in the Galaxy. Left panel: comparison between observed Θ and $v \sin i$ with the same colour and symbol scheme for T_{eff} as in Fig. 10. Middle panel: comparison between observed Θ and T_{eff} . Right panel: comparison of histograms and KDE for Θ in our sample (blue) and the one of Simón-Díaz et al. (2017) (green).

this stage, we assume equal contributions for the radial a_R and tangential a_T components of the macroturbulence to isolate possible correlations between the Θ , ξ , and $v \sin i$ parameters.

The analysis of all 57 profiles (3 values of S/N \times 16 combinations of the Θ and $v \sin i$ parameters with one fixed value of ξ , plus 3 values of S/N \times 3 combinations with varied ξ for a fixed pair of Θ and $v \sin i$) is approached with a Monte Carlo formalism. That is, each simulated profile (in other words, each combination of input parameters) is fitted multiple (200) times, where

each new fit is done after applying normally-distributed noise to the simulated profile. The fitting is being performed by minimizing a χ^2 merit function between the noisy synthetic profile and the grid of synthetic profiles covering the full parameter space. Such simulations allow for quantitative estimation of the effect of the S/N on the spread of the estimated parameters around their true value, as well as assessment of their correlations.

Figure 12 illustrates a simplified case where $v \sin i$ is fixed (under the assumption that it can be determined from an inde-

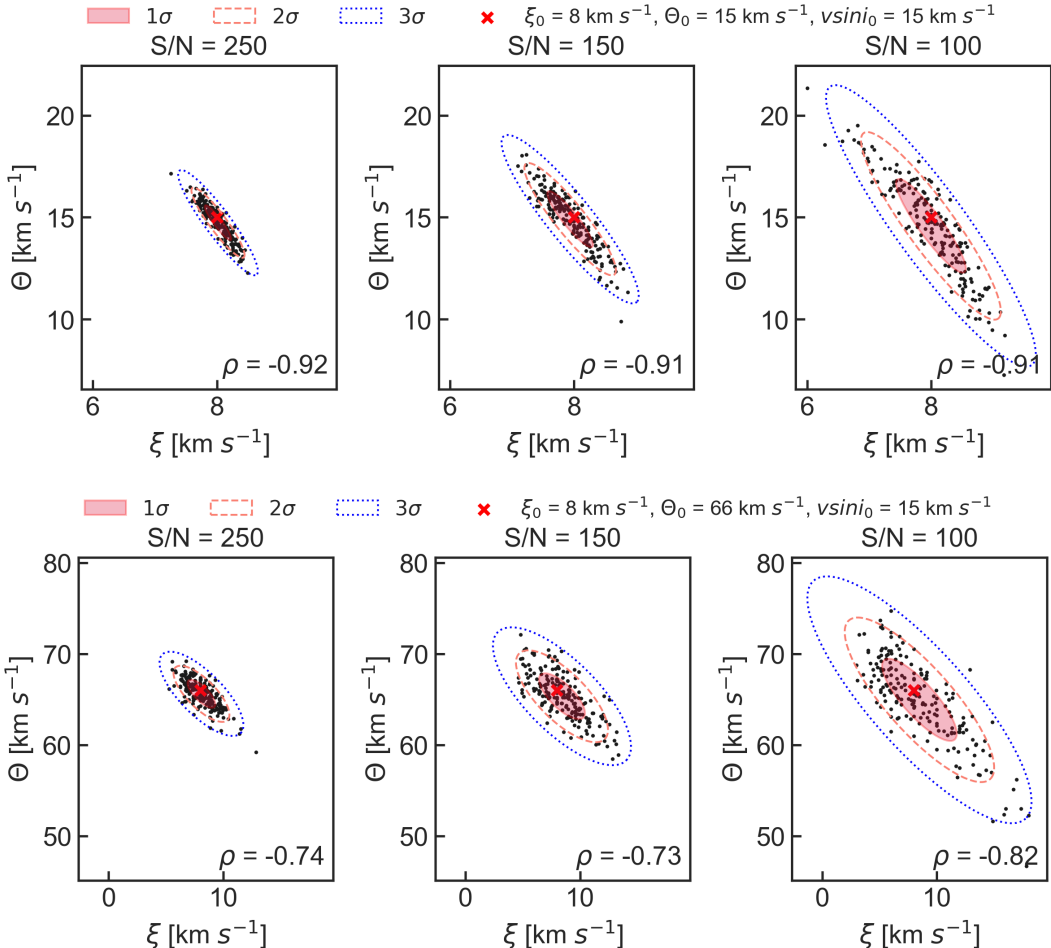


Fig. 12. Results of Monte Carlo simulations on synthetic profiles of Mg II (top set of panels) and Si III (bottom set of panels) with artificial noise (left panels: S/N = 250, middle panels: S/N = 150, and right panels: S/N = 100) with 1-, 2- and 3- σ confidence ellipses. Correlation coefficients ρ are indicated in the right corner of each panel. $v \sin i$ is fixed, while ξ and Θ are optimised. The red crosses mark true parameters of the synthetic profiles.

pendent method, such as the one based on the FT). The minimisation is performed for only two parameters, namely the micro- and macroturbulent velocities (ξ and Θ). Similar figures for other combinations with $T_{\text{eff}}=12\,000$ K (Mg II) are presented in Appendix C (Figs C.1-C.11). Plots for the case of $T_{\text{eff}}=22\,000$ K and the Si III diagnostic line are left out as they show the same trends. For a given value of the $v \sin i$ parameter and quality of the observed spectrum characterised by its S/N value, we find a strong correlation between ξ and Θ . Moreover, the correlation persists irrespective of whether the rotational broadening dominates over the macroturbulent broadening (top versus bottom row in Fig. 12). Furthermore, the 1-, 2-, and 3- σ uncertainty intervals for ξ and Θ are a strong function of the S/N value in the observed spectrum of the star (left, middle, and right columns in Fig. 12). In particular, irrespective of the assumed effective temperature of the star and accounting for the parameter correlations, we find that at the 2- σ level: (i) Θ can be inferred with a typical precision ranging from some 40% to 100% at S/N≈150 and 100, respectively, and better than some 30% at S/N≈250 when the rotational broadening dominates over macroturbulence; (ii) Θ can be inferred with precision better than 50%, 30%, and 10% at S/N≈100, 150, and 250, respectively, when the contributions from rotational broadening and macroturbu-

lence are equal; (iii) Θ can be inferred with a precision of some 20%, 10%, and 5% at S/N≈100, 150, and 250, respectively, when macroturbulence dominates over rotational broadening.

Since the described test was performed with the assumption of $v \sin i$ being known precisely, which is never the case, we now repeat the above test with one of the combinations of ξ and Θ including optimization of the third free parameter $v \sin i$, allowing it to vary in a range of typical uncertainty of the FT method (10%). The result is shown in Fig. C.12. One can see that $v \sin i$ is not significantly correlated with either ξ or Θ but introduces a spread of up to 100% in Θ , even in this case where it is varied in a limited range. Note that $v \sin i$ dominates over Θ in this instance of the test, which confirms that determination of Θ is unreliable unless it dominates over $v \sin i$.

As a further test, we now also include a tangential component of macroturbulence, a_T , as another free parameter and allow $v \sin i$ to vary. This implies we use four free parameters when fitting the line profiles: $v \sin i$, ξ , Θ , and a_T . The result is shown in Fig. C.13 for the case of S/N=250. The main conclusion is that even at such high S/N one can barely distinguish between a fit with equal radial and tangential contributions ($a_T = 0.5$) versus one with complete dominance of the tangential component ($a_T = 1.0$) at 1- σ confidence level. When allowing for 3- σ

confidence level, the solution space covers the entire range from 0 to 1 for a_T . Thus, line profiles of lower S/N do not allow to constrain this parameter observationally in case of absent independent constraints on other parameters.

6. Discussion and Conclusions

In this first paper of a series, we present a study of 124 O and B stars with unique catalog identifiers from two ESO large programmes that employ the high-resolution FEROS and UVES instruments. The sample is mostly composed of supergiants in the LMC and a few dwarfs in the Galaxy. All stars in our sample are found in the CVZ-S of the TESS space telescope and are thus potential candidates for future asteroseismic modelling, thanks to the 1-year long time base of photometric observations (Garcia et al. 2022, 2023). The same argument applies to 124 galactic dwarf stars analysed in detail in the complementary study by Gebruers et al. (2022).

We find that the reduced spectra delivered by the ESO pipeline do not meet our stringent requirements in terms of precision of the spectroscopically inferred atmospheric parameters for future asteroseismic modelling. Therefore, we develop a custom normalisation of the obtained spectra starting from the intermediate data product resulting from the ESO pipeline, that is the blaze-corrected non-merged wavelength calibrated spectra. Our tests show that a rather simple recipe of the order-by-order normalisation works well for the blue supergiants in our sample. For dwarfs, however, the same recipe fails to provide a high quality for the spectrum normalisation, most notably in the wavelength regions of the broad hydrogen lines. For those, we develop an even more sophisticated spectrum normalisation method that relies on a grid of synthetic spectra. The latter allows us to locate the local continuum and approximates the normalisation function with a series of Chebyshev polynomials.

We employ the LSD method to compute high S/N average profiles for all epochs and for all stars in our sample. We fit the obtained LSD profiles with asymmetric Gaussian functions to deduce radial velocities and the degree of asymmetry of the line profiles for each epoch. The inferred information is employed to perform a spectroscopic variability classification of the stars, where we consider four variability classes: apparently constant (“const”), spectroscopic binaries (“SB”), stars showing line profiles variations (“LPV”), and stars with line profiles characterised by an appreciable degree of skewness (“asymm”). Considering the UVES and FEROS samples separately, we find 86 apparently constant stars, 7 stars showing LPV, 28 spectroscopic binary candidates, and 37 stars exhibiting asymmetric line profiles⁹. Out of 24 stars that have both UVES and FEROS data, 20 are assigned to the same variability class. The remaining four stars, HD 268653, HD 269145, HD 269766, and HD 268675, are either classified as apparently constant based on one data set and tentatively variable in the other one, or have an extra class assignment based on either data set (see Table A.1 for details). Finally, 24 classifications are tentative and need more spectroscopic epochs for an unambiguous class assignment.

The positions of the sample stars in the spectroscopic HR diagram suggest the majority of them to be blue supergiants, with only a few objects being dwarfs situated within the SPB and β Cep instability regions. Detailed analyses of all available sectors of TESS space-based photometry is beyond the scope of

this initial spectroscopy paper but will be presented in follow-up publications. Yet, we perform a cross-match of our sample with the O- and B-type stars studied in Bowman et al. (2019a) and Bowman et al. (2020). In the observed sample, for 80% of the blue supergiants situated outside the instability regions in Fig. 6, these authors report SLF variability. One of those objects was reported to show heat-driven oscillations in TESS photometry. Only 3 of 10 stars situated within the instability regions from our spectroscopic parameters show oscillations. Validation of these initial photometric results from all available TESS sector data will be done in a dedicated follow-up study.

We employ two different methods to infer the projected rotational velocities $v \sin i$ from the spectra of the sample stars: one based on the FT of line profiles and the other one from fitting synthetic spectra to selected line profiles. Owing to the diversity of mechanisms causing the total line broadening in early-type stars, we find that the method of synthetic spectra delivers $v \sin i$ values that are either comparable to or exceed those inferred with the FT method. Therefore, we accept the FT-based $v \sin i$ measurements as the final and most precise ones in our study (see Table B.1, column “ $v \sin i_{\text{FT}}$ ”) and recommend their use in favour of those inferred from the method of synthetic spectra.

The $v \sin i$ values resulting from the FT method are subsequently used to quantify the amount of spectral line broadening due to macroturbulence for all stars in the sample. In the process, we allow $v \sin i$ to vary in a narrow range dictated by its uncertainty. We find a tendency for the macroturbulent parameter Θ to increase as the effective temperature and spectroscopic luminosity of the star increase, and that the majority of stars in the sample show macroturbulent broadening in the range between some 20 km s^{-1} and 70 km s^{-1} . Both these findings are in agreement with the results in Simón-Díaz et al. (2017) based on 430 galactic massive stars of spectral types O and B. Given that the majority of stars in our sample are in the LMC, which is characterised by a significantly lower metallicity than the galactic sample in Simón-Díaz et al. (2017), we conclude that the observed macroturbulence in spectral lines of massive stars does not depend on their bulk metallicity (taking into account our smaller sample size and dominance by evolved objects). Furthermore, we check for a possible correlation between the inferred macroturbulent velocity parameter and the variability class we have assigned to our targets (cf. Table A.1). In this exercise, we consider the following groups of stars: (i) “const” versus all other groups together, (ii) “const” versus “asym”, (iii) “const” versus “lpv”, and (iv) “asym” versus “lpv”. We could not identify any correlation between the macroturbulent velocity and the class of spectroscopic variability.

In an attempt to quantify the two individual contributions known as the radial and tangential components of macroturbulence from spectral line fitting, we find the results to be sensitive to the initial guess for the respective parameters a_R and a_T ¹⁰. Although the obtained distribution is skewed towards $a_T \gtrsim 0.6$, we cannot firmly conclude to observe a dominant tangential component given the limited quality of our spectroscopic data in terms of S/N. When all the assumptions of our approach are met, that is (i) a fixed microturbulent velocity ξ typical for given spectral type applies; (ii) $v \sin i$ inferred from Fourier transforms of observed profiles varies modestly; (iii) the initial guess for a_T is not lower than 0.4, one may conclude that the tangential component a_T is larger than the radial one in our sample. This may possibly be an indicator of broadening by gravity or gravito-inertial

⁹ The total number of classifications exceeds the sample size of 148 objects because some of the stars are assigned to two variability classes (see Table A.1).

¹⁰ Note that we optimise the a_T parameter only while the contribution of the radial component is set according to $a_R = 1 - a_T$ (see Sect. 4.4).

waves (Aerts et al. 2023). This interpretation should be treated with caution since any meaningful inference for the individual radial and tangential components of the macroturbulent broadening requires $S/N \geq 250$ (see Sect. 5).

Finally, we add a word of caution to the way uncertainties are estimated for the macroturbulent velocity parameter Θ in the literature. The commonly accepted approach, and the one employed in this work too, is to decouple the inferences of the macro- and microturbulent broadening parameters, where the latter is usually optimised together with the effective temperature and surface gravity of the star. Our study shows that the Θ and ξ parameters are strongly correlated for the case of massive stars. Hence, fixing the microturbulent velocity parameter ξ while quantifying contribution of macroturbulence to the line broadening results in underestimation of the uncertainties for the latter. Furthermore, the precision with which the macroturbulent broadening parameter Θ can be inferred depends strongly on the S/N of the spectra, as well as on the dominant line broadening mechanism among rotation or macroturbulence. The uncertainty on the Θ parameter increases progressively as the dominance of the projected rotational velocity $v \sin i$ grows. These findings are in agreement with the results obtained in Simón-Díaz et al. (2017), where the authors report only the upper limit for the macroturbulence parameter for the majority of stars with $v \sin i > \Theta$.

Future studies of all stars in the combined UVES and FEROS samples will be focused on detailed analyses of their atmospheric chemical compositions and frequency analyses based on all TESS data that will be available by the time. Subsequently, we will also perform detailed asteroseismic modelling for stars with sufficient identified oscillation modes, relying on the spectroscopic constraints offered in this work and from the future results for the individual elemental abundances.

Acknowledgements. The research leading to these results has received funding from the KU Leuven Research Council (grant C16/18/005: PARADISE), from the Research Foundation Flanders (FWO) under grant agreements G089422N (NS, CA, AT), K802922N (CA, Sabbatical leave), 11E5620N (SG, PhD Aspirant mandate), 1124321N (LJ, PhD Aspirant mandate), 12ZB620N (TVR, Junior Postdoctoral Fellowship), and 1286521N (DMB, Senior Postdoctoral Fellowship), as well as from the BELgian federal Science Policy Office (BELSPO) through PRODEX grant PLATO. This research has made use of the SIMBAD database, operated at CDS, Strasbourg, France. The TESS data presented in this paper were obtained from the Mikulski Archive for Space Telescopes (MAST) at the Space Telescope Science Institute (STScI), which is operated by the Association of Universities for Research in Astronomy, Inc., under NASA contract NAS5-26555. Support to MAST for these data is provided by the NASA Office of Space Science via grant NAG5-7584 and by other grants and contracts. Funding for the TESS mission is provided by the NASA Explorer Program.

References

- Aerts, C. 2021, *Reviews of Modern Physics*, 93, 015001
 Aerts, C., Bowman, D. M., Simón-Díaz, S., et al. 2018, *MNRAS*, 476, 1234
 Aerts, C., Briquet, M., Degroote, P., Thoul, A., & van Hoolst, T. 2011, *A&A*, 534, A98
 Aerts, C., Christensen-Dalsgaard, J., & Kurtz, D. W. 2010a, *Asteroseismology (Astronomy and Astrophysics Library)*. ISBN 978-1-4020-5178-4. Springer Science+Business Media
 Aerts, C., De Cat, P., Peeters, E., et al. 1999, *A&A*, 343, 872
 Aerts, C. & Kolenberg, K. 2005, *A&A*, 431, 615
 Aerts, C., Lefever, K., Baglin, A., et al. 2010b, *A&A*, 513, L11
 Aerts, C., Mathis, S., & Rogers, T. M. 2019, *ARA&A*, 57, 35
 Aerts, C., Moltenberghs, G., & De Ridder, J. 2023, *A&A*, 672, A183
 Aerts, C., Puls, J., Godart, M., & Dupret, M. A. 2009, *A&A*, 508, 409
 Aerts, C. & Rogers, T. M. 2015, *ApJ*, 806, L33
 Aerts, C., Simón-Díaz, S., Bloemen, S., et al. 2017a, *A&A*, 602, A32
 Aerts, C., Simón-Díaz, S., Groot, P. J., & Degroote, P. 2014, *A&A*, 569, A118
 Aerts, C., Thoul, A., Daszyńska, J., et al. 2003, *Science*, 300, 1926
 Aerts, C., Van Reeth, T., & Tkachenko, A. 2017b, *ApJ*, 847, L7
 Auvergne, M., Bodin, P., Boisnard, L., et al. 2009, *A&A*, 506, 411
 Balona, L. A. 2014, *MNRAS*, 437, 1476
 Balona, L. A., Daszyńska-Daszkiewicz, J., & Pamyatnykh, A. A. 2015, *MNRAS*, 452, 3073
 Balona, L. A. & Ozuyar, D. 2020, *MNRAS*, 493, 5871
 Beck, P. G., Montalban, J., Kallinger, T., et al. 2012, *Nature*, 481, 55
 Belkacem, K., Dupret, M. A., & Noels, A. 2010, *A&A*, 510, A6
 Belkacem, K., Samadi, R., Goupil, M.-J., et al. 2009, *Science*, 324, 1540
 Blomme, R., Mahy, L., Catala, C., et al. 2011, *A&A*, 533, A4
 Borucki, W. J., Koch, D., Basri, G., et al. 2010, *Science*, 327, 977
 Bouabid, M. P., Dupret, M. A., Salmon, S., et al. 2013, *MNRAS*, 429, 2500
 Bowman, D. M. 2020, *Frontiers in Astronomy and Space Sciences*, 7, 70
 Bowman, D. M., Aerts, C., Johnston, C., et al. 2019, *A&A*, 621, A135
 Bowman, D. M., Burssens, S., Pedersen, M. G., et al. 2019a, *Nature Astronomy*, 3, 760
 Bowman, D. M., Burssens, S., Simón-Díaz, S., et al. 2020, *A&A*, 640, A36
 Bowman, D. M. & Dorn-Wallenstein, T. Z. 2022, *A&A*, 668, A134
 Bowman, D. M., Johnston, C., Tkachenko, A., et al. 2019b, *ApJ*, 883, L26
 Bowman, D. M. & Kurtz, D. W. 2018, *MNRAS*, 476, 3169
 Bowman, D. M. & Michelsen, M. 2021, *A&A*, 656, A158
 Brahm, R., Jordán, A., & Espinoza, N. 2017, *PASP*, 129, 034002
 Briquet, M., Aerts, C., Baglin, A., et al. 2011, *A&A*, 527, A112
 Briquet, M., Neiner, C., Aerts, C., et al. 2012, *MNRAS*, 427, 483
 Burssens, S., Simón-Díaz, S., Bowman, D. M., et al. 2020, *A&A*, 639, A81
 Buyschaert, B., Aerts, C., Bloemen, S., et al. 2015, *MNRAS*, 453, 89
 Buyschaert, B., Aerts, C., Bowman, D. M., et al. 2018, *A&A*, 616, A148
 Cantiello, M., Langer, N., Brott, I., et al. 2009, *A&A*, 499, 279
 Cantiello, M., Lecoanet, D., Jermyn, A. S., & Grassitelli, L. 2021, *ApJ*, 915, 112
 Cantiello, M., Mankovich, C., Bildsten, L., Christensen-Dalsgaard, J., & Paxton, B. 2014, *ApJ*, 788, 93
 Carroll, J. A. 1933, *MNRAS*, 93, 478
 Cheng, S. J., Fuller, J., Guo, Z., Lehman, H., & Hambleton, K. 2020, *ApJ*, 903, 122
 Choudhury, S., de Grij, R., Bekki, K., et al. 2021, *MNRAS*, 507, 4752
 Claret, A. & Bloemen, S. 2011, *A&A*, 529, A75
 Claret, A. & Torres, G. 2018, *The Astrophysical Journal*, 859, id.100
 Claret, A. & Torres, G. 2019, *ApJ*, 876, 134
 Conn, A. R., Gould, N. I. M., & Toint, P. L. 2000, *Trust Region Methods* (Society for Industrial and Applied Mathematics)
 De Cat, P. & Aerts, C. 2002, *A&A*, 393, 965
 Deal, M., Escobar, M. E., Vauclair, S., et al. 2017, *A&A*, 601, A127
 Deal, M., Richard, O., & Vauclair, S. 2016, *A&A*, 589, A140
 Degroote, P., Aerts, C., Baglin, A., et al. 2010a, *Nature*, 464, 259
 Degroote, P., Briquet, M., Auvergne, M., et al. 2010b, *A&A*, 519, A38
 Degroote, P., Briquet, M., Catala, C., et al. 2009, *A&A*, 506, 111
 Deheuvels, S., Ballot, J., Eggenberger, P., et al. 2020, *A&A*, 641, A117
 Deheuvels, S., Brandão, I., Silva Aguirre, V., et al. 2016, *A&A*, 589, A93
 Dekker, H., D'Odorico, S., Kaufer, A., Delabre, B., & Kotzlowski, H. 2000, in *Society of Photo-Optical Instrumentation Engineers (SPIE) Conference Series*, Vol. 4008, *Optical and IR Telescope Instrumentation and Detectors*, ed. M. Iye & A. F. Moorwood, 534–545
 Diago, P. D., Gutiérrez-Soto, J., Auvergne, M., et al. 2009, *A&A*, 506, 125
 Donati, J. F., Semel, M., Carter, B. D., Rees, D. E., & Collier Cameron, A. 1997, *MNRAS*, 291, 658
 Dziembowski, W. A. & Pamyatnykh, A. A. 2008, *MNRAS*, 385, 2061
 Edelmann, P. V. F., Ratnasingam, R. P., Pedersen, M. G., et al. 2019, *ApJ*, 876, 4
 Freudling, W., Romaniello, M., Bramich, D. M., et al. 2013, *A&A*, 559, A96
 Fuller, J. 2017, *MNRAS*, 472, 1538
 Fuller, J. 2021, *MNRAS*, 501, 483
 Fuller, J., Hambleton, K., Shporer, A., Isaacson, H., & Thompson, S. 2017, *MNRAS*, 472, L25
 Fuller, J., Kurtz, D. W., Handler, G., & Rappaport, S. 2020, *MNRAS*, 498, 5730
 Fuller, J. & Lai, D. 2012, *MNRAS*, 420, 3126
 Gaia Collaboration, De Ridder, J., Ripepi, V., et al. 2022, *A&A*, in press
 Garcia, S., Van Reeth, T., De Ridder, J., & Aerts, C. 2023, *A&A*, in press, arXiv:2210.09526
 Garcia, S., Van Reeth, T., De Ridder, J., et al. 2022, *A&A*, 662, A82
 Gebruers, S., Tkachenko, A., Bowman, D., et al. 2022, submitted to *A&A*
 Gray, D. F. 2008, *The Observation and Analysis of Stellar Photospheres*
 Gray, R. O. & Corbally, Christopher, J. 2009, *Stellar Spectral Classification*
 Grevesse, N., Asplund, M., & Sauval, A. J. 2007, *Space Sci. Rev.*, 130, 105
 Guo, Z. 2021, *Frontiers in Astronomy and Space Sciences*, 8, 67
 Guo, Z., Fuller, J., Shporer, A., et al. 2019, *ApJ*, 885, 46
 Guo, Z., Shporer, A., Hambleton, K., & Isaacson, H. 2020, *ApJ*, 888, 95
 Gutiérrez-Soto, J., Floquet, M., Samadi, R., et al. 2009, *A&A*, 506, 133
 Hambleton, K., Kurtz, D. W., Prša, A., et al. 2016, *MNRAS*, 463, 1199
 Hambleton, K. M., Kurtz, D. W., Prša, A., et al. 2013, *MNRAS*, 434, 925
 Handler, G., Jerzykiewicz, M., Rodríguez, E., et al. 2006, *MNRAS*, 365, 327
 Handler, G., Kurtz, D. W., Rappaport, S. A., et al. 2020, *Nature Astronomy*, 4, 684

- Handler, G., Matthews, J. M., Eaton, J. A., et al. 2009, *ApJ*, 698, L56
- Hekker, S. & Christensen-Dalsgaard, J. 2017, *A&A Rev.*, 25, 1
- Hermes, J. J., Gänsicke, B. T., Kawaler, S. D., et al. 2017, *ApJS*, 232, 23
- Hillier, D. J. & Miller, D. L. 1998, *ApJ*, 496, 407
- Holgado, G., Simón-Díaz, S., Barbá, R. H., et al. 2018, *A&A*, 613, A65
- Horst, L., Edelmann, P. V. F., András, R., et al. 2020, *A&A*, 641, A18
- Huat, A. L., Hubert, A. M., Baudin, F., et al. 2009, *A&A*, 506, 95
- Hunter, I., Lennon, D. J., Dufton, P. L., et al. 2008, *A&A*, 479, 541
- IJspeert, L. W., Tkachenko, A., Johnston, C., et al. 2021, *A&A*, 652, A120
- Jayaraman, R., Handler, G., Rappaport, S. A., et al. 2022, *ApJ*, 928, L14
- Johnston, C. 2021, *A&A*, 655, A29
- Kaufer, A., Stahl, O., Tubbesing, S., et al. 1999, *The Messenger*, 95, 8
- Kołaczk-Szymański, P. A., Pigulski, A., Michalska, G., Moździerski, D., & Różański, T. 2021, *A&A*, 647, A12
- Kurtz, D. W. 2022, *Annual Review of Astronomy and Astrophysics*, 60, 31
- Kurtz, D. W., Handler, G., Rappaport, S. A., et al. 2020, *MNRAS*, 494, 5118
- Lampens, P. 2021, *Galaxies*, 9, 28
- Lanz, T. & Hubeny, I. 2003, *ApJS*, 146, 417
- Lanz, T. & Hubeny, I. 2007, *ApJS*, 169, 83
- Lecoanet, D., Bowman, D. M., & Van Reeth, T. 2022, *MNRAS*, 512, L16
- Lecoanet, D., Cantiello, M., Quataert, E., et al. 2019, *ApJ*, 886, L15
- Lee, J. W. 2021, *PASJ*, 73, 809
- Li, G., Van Reeth, T., Bedding, T. R., et al. 2020, *MNRAS*, 491, 3586
- Maceroni, C., Montalbán, J., Michel, E., et al. 2009, *A&A*, 508, 1375
- Mahy, L., Almeida, L. A., Sana, H., et al. 2020a, *A&A*, 634, A119
- Mahy, L., Gosset, E., Baudin, F., et al. 2011, *A&A*, 525, A101
- Mahy, L., Sana, H., Abdul-Masih, M., et al. 2020b, *A&A*, 634, A118
- Martins, F. & Palacios, A. 2013, *A&A*, 560, A16
- Maxted, P. F. L., Gaulme, P., Graczyk, D., et al. 2020, *MNRAS*, 498, 332
- Maxted, P. F. L. & Hutcheon, R. J. 2018, *A&A*, 616, A38
- Michelsen, M., Aerts, C., & Bowman, D. M. 2021, *A&A*, 650, A175
- Michelsen, M., Pedersen, M. G., Augustson, K. C., Mathis, S., & Aerts, C. 2019, *A&A*, 628, A76
- Miglio, A., Montalbán, J., Noels, A., & Eggenberger, P. 2008, *MNRAS*, 386, 1487
- Mombarg, J. S. G., Dotter, A., Rieutord, M., et al. 2022, *ApJ*, 925, 154
- Mombarg, J. S. G., Dotter, A., Van Reeth, T., et al. 2020, *ApJ*, 895, 51
- Mombarg, J. S. G., Van Reeth, T., & Aerts, C. 2021, *A&A*, 650, A58
- Mombarg, J. S. G., Van Reeth, T., Pedersen, M. G., et al. 2019, *MNRAS*, 485, 3248
- Moravveji, E., Aerts, C., Pápics, P. I., Triana, S. A., & Vandoren, B. 2015, *A&A*, 580, A27
- Moravveji, E., Townsend, R. H. D., Aerts, C., & Mathis, S. 2016, *ApJ*, 823, 130
- Mosser, B., Goupil, M. J., Belkacem, K., et al. 2012, *A&A*, 548, A10
- Mowlavi, N., Barblan, F., Saesen, S., & Eyer, L. 2013, *A&A*, 554, A108
- Mowlavi, N., Saesen, S., Semaan, T., et al. 2016, *A&A*, 595, L1
- Moździerski, D., Pigulski, A., Kołaczkowski, Z., et al. 2019, *A&A*, 632, A95
- Moździerski, D., Pigulski, A., Kopacki, G., Kołaczkowski, Z., & Stęślicki, M. 2014, *Acta Astron.*, 64, 89
- Murphy, S. J., Hey, D., Van Reeth, T., & Bedding, T. R. 2019, *MNRAS*, 485, 2380
- Neiner, C., Gutiérrez-Soto, J., Baudin, F., et al. 2009, *A&A*, 506, 143
- Neiner, C., Mathis, S., Saio, H., et al. 2012, *A&A*, 539, A90
- Ouazzani, R. M., Lignières, F., Dupret, M. A., et al. 2020, *A&A*, 640, A49
- Ouazzani, R. M., Marques, J. P., Goupil, M. J., et al. 2019, *A&A*, 626, A121
- Ouazzani, R.-M., Salmon, S. J. A. J., Antoci, V., et al. 2017, *MNRAS*, 465, 2294
- Pápics, P. I., Tkachenko, A., Van Reeth, T., et al. 2017, *A&A*, 598, A74
- Pavlovski, K., Hummel, C. A., Tkachenko, A., et al. 2022, *A&A*, 658, A92
- Pedersen, M. G. 2022, *The Astrophysical Journal*, 930, 94
- Pedersen, M. G., Aerts, C., Pápics, P. I., et al. 2021, *Nature Astronomy*, 5, 715
- Pedersen, M. G., Aerts, C., Pápics, P. I., & Rogers, T. M. 2018, *A&A*, 614, A128
- Pedersen, M. G., Chowdhury, S., Johnston, C., et al. 2019, *ApJ*, 872, L9
- Rappaport, S. A., Kurtz, D. W., Handler, G., et al. 2021, *MNRAS*, 503, 254
- Ratnasingam, R. P., Edelmann, P. V. F., & Rogers, T. M. 2020, *MNRAS*, 497, 4231
- Ricker, G. R., Winn, J. N., Vanderspek, R., et al. 2015, *Journal of Astronomical Telescopes, Instruments, and Systems*, 1, id. 014003
- Rogers, T. M., Lin, D. N. C., McElwaine, J. N., & Lau, H. H. B. 2013, *ApJ*, 772, 21
- Saesen, S., Briquet, M., Aerts, C., Miglio, A., & Carrier, F. 2013, *AJ*, 146, 102
- Saesen, S., Carrier, F., Pigulski, A., et al. 2010, *A&A*, 515, A16
- Salmon, S. J. A. J., Montalbán, J., Reese, D. R., Dupret, M. A., & Eggenberger, P. 2014, *A&A*, 569, A18
- Serenelli, A., Weiss, A., Aerts, C., et al. 2021, *A&A Rev.*, 29, 4
- Sharma, A. N., Bedding, T. R., Saio, H., & White, T. R. 2022, *Monthly Notices of the Royal Astronomical Society*, 515, 828
- Simón-Díaz, S., Aerts, C., Urbaneja, M. A., et al. 2018, *A&A*, 612, A40
- Simón-Díaz, S., Godart, M., Castro, N., et al. 2017, *A&A*, 597, A22
- Simón-Díaz, S. & Herrero, A. 2014, *A&A*, 562, A135
- Southworth, J. 2021, *Universe*, 7, 369
- Straumit, I., Tkachenko, A., Gebruers, S., et al. 2022, *The Astronomical Journal*, 163, 236
- Szewczuk, W. & Daszyńska-Daszkiewicz, J. 2018, *MNRAS*, 478, 2243
- Szewczuk, W., Walczak, P., & Daszyńska-Daszkiewicz, J. 2021, *MNRAS*, 503, 5894
- Szewczuk, W., Walczak, P., Daszyńska-Daszkiewicz, J., & Moździerski, D. 2022, *MNRAS*, 511, 1529
- Takeda, Y. & UeNo, S. 2017, *Publications of the Astronomical Society of Japan*, 69
- Telting, J. H., Schrijvers, C., Ilyin, I. V., et al. 2006, *A&A*, 452, 945
- Thompson, S. E., Everett, M., Mullally, F., et al. 2012, *ApJ*, 753, 86
- Thoul, A., Degroote, P., Catala, C., et al. 2013, *A&A*, 551, A12
- Tkachenko, A. 2015, *A&A*, 581, A129
- Tkachenko, A., Pavlovski, K., Johnston, C., et al. 2020, *A&A*, 637, A60
- Tkachenko, A., Van Reeth, T., Tsymbal, V., et al. 2013, *A&A*, 560, A37
- Triana, S. A., Moravveji, E., Pápics, P. I., et al. 2015, *ApJ*, 810, 16
- Uytterhoeven, K., Moya, A., Grigahcène, A., et al. 2011, *A&A*, 534, A125
- Van Eylen, V., Winn, J. N., & Albrecht, S. 2016, *ApJ*, 824, 15
- Van Reeth, T., Mombarg, J. S. G., Mathis, S., et al. 2018, *A&A*, 618, A24
- Van Reeth, T., Southworth, J., Van Beeck, J., & Bowman, D. M. 2022, *A&A*, 659, A177
- Van Reeth, T., Tkachenko, A., & Aerts, C. 2016, *A&A*, 593, A120
- Van Reeth, T., Tkachenko, A., Aerts, C., et al. 2015a, *A&A*, 574, A17
- Van Reeth, T., Tkachenko, A., Aerts, C., et al. 2015b, *ApJS*, 218, 27
- Welsh, W. F., Orosz, J. A., Aerts, C., et al. 2011, *ApJS*, 197, 4
- Wenger, M., Ochsenbein, F., Egret, D., et al. 2000, *A&AS*, 143, 9
- Zahn, J.-P. 2013, in *Lecture Notes in Physics*, Berlin Springer Verlag, ed. J. Souchay, S. Mathis, & T. Tokieda, Vol. 861, 301

Appendix A: Results of the global stellar parameter estimations

Table A.1. Results of the spectrum analysis and respective spectroscopic classification of stars in the combined UVES and FEROS sample. The “?” mark indicates ambiguous classifications. For example, the star is classified as “SB1?” when the detected RV difference between the two observed epochs exceeds mildly the 3σ uncertainty interval and no large asymmetries are detected in the line profiles. Superscripts “a”, “b”, “c” refer respectively to the GSSP, TLUSTY, and CMFGEN models employed for the spectrum analysis of the sample stars.

Object name	Spectral class	T_{eff} (K)	$\log g$ (dex)	RV_1 (km s^{-1})	ΔRV	Asymmetry_1	Asymmetry_2	Variability
UVES								
SK -71 51 ^b	O6V	47480 ± 3210	3.72 ± 0.20	206.6 ± 9.6	19.7 ± 18.0	0.81 ± 0.16	1.18 ± 0.24	asymm?
HT 83 alf ^b	O6V	47440 ± 3490	3.70 ± 0.20	296.2 ± 8.1	3.6 ± 16.8	1.14 ± 0.18	0.97 ± 0.15	asymm?
BI 42 ^b	O9V	33760 ± 1940	3.59 ± 0.24	283.5 ± 3.5	3.7 ± 6.8	1.02 ± 0.08	0.82 ± 0.06	const
HD 269525 ^b	B0I	32300 ± 1100	3.24 ± 0.20	309.7 ± 4.5	4.5 ± 9.4	-1.01 ± 0.11	-1.0 ± 0.11	const
SK -66 138 ^b	O9.5III	30410 ± 1190	3.32 ± 0.18	307.6 ± 2.5	1.5 ± 4.8	1.17 ± 0.09	1.15 ± 0.09	const
RMC 95 ^b	B0I	28890 ± 1430	3.16 ± 0.16	311.6 ± 1.9	0.9 ± 3.7	1.11 ± 0.06	-1.17 ± 0.06	const
RMC 93 ^b	B0II	28650 ± 1620	3.13 ± 0.18	297.3 ± 3.5	9.6 ± 6.7	-0.63 ± 0.04	1.04 ± 0.07	asymm
BI 188 ^b	B0I	27720 ± 1240	3.11 ± 0.19	250.9 ± 2.3	7.6 ± 4.3	1.37 ± 0.08	1.3 ± 0.08	const
HD 269769 ^b	B0I	27540 ± 860	3.04 ± 0.12	282.7 ± 1.6	9.5 ± 4.0	1.22 ± 0.06	1.12 ± 0.06	asymm
SK -70 13 ^b	O9.5I	26550 ± 1990	2.96 ± 0.15	258.0 ± 2.0	3.5 ± 4.1	1.03 ± 0.06	1.23 ± 0.08	const
RMC 97 ^b	B0.5Ib	25020 ± 2310	3.11 ± 0.23	325.8 ± 1.8	3.6 ± 3.6	1.36 ± 0.06	1.33 ± 0.07	asymm?LPV?
SK -66 15 ^b	B0.5I	24550 ± 2070	2.82 ± 0.20	284.0 ± 1.2	3.0 ± 2.6	0.96 ± 0.04	0.92 ± 0.04	const
SK -69 180 ^b	B1I	24000 ± 2210	2.90 ± 0.20	272.0 ± 1.1	1.7 ± 2.4	0.94 ± 0.04	0.92 ± 0.04	const
SK -67 54 ^b	B0.5I	23880 ± 2160	2.76 ± 0.22	306.6 ± 1.1	0.5 ± 2.3	1.07 ± 0.04	0.94 ± 0.04	const
SK -69 275 ^b	B1I	23800 ± 3160	2.90 ± 0.24	252.1 ± 1.3	6.6 ± 2.7	1.26 ± 0.06	1.12 ± 0.05	const
MCPS 082.95108-69.23933 ^b	B1I	23670 ± 2170	2.88 ± 0.21	290.4 ± 1.2	0.7 ± 2.4	1.13 ± 0.05	1.08 ± 0.05	const
HD 269700 ^b	B1.5	23010 ± 660	2.38 ± 0.20	276.8 ± 1.3	15.0 ± 2.4	1.93 ± 0.1	1.95 ± 0.1	asymm
CPD-69 457 ^b	B0.5I	23000 ± 600	2.46 ± 0.20	293.1 ± 1.5	6.2 ± 3.1	1.14 ± 0.06	1.33 ± 0.08	SB1?
SK -68 147 ^b	B1I	22900 ± 2420	2.84 ± 0.22	291.7 ± 0.9	2.4 ± 2.0	0.97 ± 0.04	0.88 ± 0.04	const
Dachs LMC 2-19 ^b	B1I	22640 ± 2370	2.76 ± 0.21	306.0 ± 1.6	3.3 ± 2.9	1.14 ± 0.06	1.16 ± 0.06	const
HD 269314 ^b	B0I	22560 ± 660	2.48 ± 0.20	301.6 ± 1.7	3.2 ± 3.6	1.18 ± 0.06	1.05 ± 0.05	const
CPD-69 445 ^b	B1I	22480 ± 2100	2.62 ± 0.18	262.0 ± 1.4	1.1 ± 3.0	1.15 ± 0.05	1.05 ± 0.05	const
SK -69 256 ^b	B1I	22380 ± 1960	2.66 ± 0.17	241.7 ± 1.6	10.9 ± 2.9	0.9 ± 0.05	1.25 ± 0.06	asymm
RMC 142 ^b	B0I	22180 ± 650	2.43 ± 0.20	270.2 ± 1.3	8.2 ± 2.4	1.64 ± 0.09	1.48 ± 0.08	asymm
HD 269859 ^b	B0I	22000 ± 770	2.10 ± 0.20	279.6 ± 0.9	1.2 ± 1.7	1.41 ± 0.06	1.57 ± 0.06	asymm
HD 270754 ^b	B1I	22000 ± 700	2.48 ± 0.20	321.5 ± 0.8	2.3 ± 1.8	1.4 ± 0.05	1.51 ± 0.06	asymm
HD 270196 ^b	B1I	22000 ± 650	2.39 ± 0.20	239.8 ± 1.0	1.3 ± 2.0	1.08 ± 0.04	1.01 ± 0.04	const
SK -67 46 ^b	B1.5I	22000 ± 2300	2.62 ± 0.20	310.0 ± 1.1	2.3 ± 2.3	1.03 ± 0.04	1.17 ± 0.05	const
SK -69 167 ^b	B1I	21890 ± 1960	2.68 ± 0.16	278.2 ± 1.4	4.9 ± 2.6	1.1 ± 0.06	1.3 ± 0.06	const
HD 269786 ^b	B1I	21870 ± 730	2.46 ± 0.20	288.4 ± 1.0	4.3 ± 1.9	1.64 ± 0.07	1.25 ± 0.05	asymm
SK -67 76 ^b	B0I	21860 ± 1040	2.11 ± 0.20	322.9 ± 1.8	1.1 ± 3.6	1.16 ± 0.07	1.38 ± 0.08	asymm
HD 269655 ^b	B0I	21780 ± 780	2.33 ± 0.20	278.4 ± 1.0	12.2 ± 2.6	1.24 ± 0.05	1.51 ± 0.07	asymm
SK -69- 157 ^b	B1I	21770 ± 1440	2.55 ± 0.20	257.8 ± 1.4	4.5 ± 2.7	1.13 ± 0.05	1.1 ± 0.05	const
HD 269660 ^b	B2I	21690 ± 700	2.45 ± 0.20	247.4 ± 1.0	0.4 ± 1.8	0.99 ± 0.04	1.15 ± 0.04	const
SK -69 68 ^b	B1I	21660 ± 760	2.18 ± 0.20	243.3 ± 1.2	14.5 ± 2.2	1.25 ± 0.04	1.11 ± 0.03	asymm
HD 268809 ^b	B1I	21480 ± 730	2.13 ± 0.20	239.5 ± 1.1	15.1 ± 2.2	0.95 ± 0.04	1.21 ± 0.05	asymm?
LH 47-373A ^b	B1I	21320 ± 760	2.48 ± 0.20	312.0 ± 1.2	1.6 ± 2.3	0.91 ± 0.04	1.13 ± 0.04	const
HD 268623 ^b	B1I	20920 ± 870	2.48 ± 0.20	284.9 ± 1.0	6.9 ± 2.1	1.18 ± 0.05	1.12 ± 0.05	SB1?
SK -68 17 ^b	B4I	20850 ± 1660	2.68 ± 0.18	272.4 ± 1.0	2.8 ± 1.9	1.05 ± 0.04	1.1 ± 0.04	const
W61 27-5 ^b	B1I	20760 ± 860	2.12 ± 0.20	281.2 ± 1.0	5.1 ± 2.1	0.93 ± 0.04	1.13 ± 0.05	const
HD 268798 ^b	B2I	20250 ± 1210	2.04 ± 0.18	278.4 ± 1.0	8.3 ± 1.8	0.96 ± 0.03	1.09 ± 0.04	SB1?asymm?
CPD-68 309 ^b	B2.5I	19290 ± 630	2.12 ± 0.20	255.4 ± 0.6	4.6 ± 1.2	1.24 ± 0.04	1.18 ± 0.04	SB1?
SK -68 27 ^b	B3I	18630 ± 1880	2.50 ± 0.23	285.0 ± 1.0	1.9 ± 2.1	1.14 ± 0.04	0.99 ± 0.04	const
HD 269845 ^b	B2I	18590 ± 1610	2.40 ± 0.16	300.0 ± 0.8	0.7 ± 1.7	1.25 ± 0.04	1.01 ± 0.04	const
SK -68 2 ^b	B9.5Iab	18420 ± 1850	2.37 ± 0.20	285.6 ± 1.0	1.6 ± 2.2	1.14 ± 0.04	1.26 ± 0.06	const
HD 268653 ^b	B2I	18090 ± 940	2.12 ± 0.15	306.1 ± 0.9	0.4 ± 1.7	1.41 ± 0.05	1.31 ± 0.04	asymm?
HD 269992 ^b	B2I	18070 ± 1110	2.24 ± 0.19	249.2 ± 0.7	7.1 ± 1.5	1.13 ± 0.04	1.18 ± 0.04	asymm?
HD 269997 ^b	B2.5I	17000 ± 1730	2.16 ± 0.21	262.7 ± 0.8	6.7 ± 1.6	1.21 ± 0.04	1.19 ± 0.04	SB1?
HD 269101 ^b	B3I	17000 ± 1530	2.26 ± 0.16	303.3 ± 0.9	0.7 ± 1.8	1.2 ± 0.05	1.12 ± 0.04	const
SK -67 133 ^c	B2.5Iab	16630 ± 850	2.28 ± 0.12	298.9 ± 1.0	2.2 ± 2.0	1.33 ± 0.06	1.27 ± 0.05	const
HD 268729 ^b	B5I	16420 ± 780	1.95 ± 0.20	242.4 ± 0.8	29.3 ± 1.7	0.88 ± 0.04	1.13 ± 0.04	SB1
HD 271213 ^c	B2I	16250 ± 600	2.18 ± 0.20	245.4 ± 1.0	0.4 ± 2.0	1.19 ± 0.05	1.38 ± 0.06	const
HD 270949 ^c	B5I	15900 ± 580	1.96 ± 0.20	298.4 ± 1.0	3.8 ± 1.9	1.11 ± 0.04	1.27 ± 0.05	SB1?asymm?

Table A.1. continued.

Object name	Spectral class	T_{eff} (K)	$\log g$ (dex)	RV_1 (km s^{-1})	ΔRV	Asymmetry_1	Asymmetry_2	Variability
HD 269145 ^c	B5I	15860 ± 560	1.94 ± 0.20	308.2 ± 0.9	10.2 ± 1.7	-1.0 ± 0.04	1.11 ± 0.04	SB1?
HD 269920 ^c	B3I	15560 ± 560	1.97 ± 0.20	280.3 ± 0.9	4.4 ± 1.8	1.13 ± 0.05	1.17 ± 0.05	const
HD 269854 ^b	B5I	15340 ± 690	1.98 ± 0.20	294.2 ± 1.1	1.9 ± 2.3	1.17 ± 0.06	1.24 ± 0.07	const
SK -70 53 ^b	B5I	15340 ± 1300	2.28 ± 0.17	252.4 ± 0.9	1.1 ± 1.8	1.1 ± 0.05	1.08 ± 0.05	const
SK -67 275 ^c	B6I	14960 ± 890	2.23 ± 0.16	294.7 ± 1.2	4.1 ± 2.4	1.45 ± 0.07	1.55 ± 0.07	asymm
SK -67 283 ^c	B6I	14880 ± 800	2.26 ± 0.14	295.5 ± 1.1	5.5 ± 2.3	1.27 ± 0.07	1.08 ± 0.06	const
HD 47620 ^a	B6V	14850 ± 740	3.97 ± 0.18	38.2 ± 2.5	2.9 ± 4.7	1.3 ± 0.16	0.89 ± 0.12	LPV
SK -66 125 ^c	B4I	14830 ± 760	2.34 ± 0.13	309.1 ± 0.9	2.5 ± 1.8	1.13 ± 0.06	1.05 ± 0.06	const
HD 269644 ^c	B6I	14770 ± 500	1.94 ± 0.20	306.7 ± 0.9	0.2 ± 1.8	0.98 ± 0.05	0.94 ± 0.05	const
SK -67 127 ^c	B6I	14750 ± 880	2.09 ± 0.14	314.4 ± 1.2	1.8 ± 2.3	0.95 ± 0.06	1.07 ± 0.07	const
HD 268907 ^c	B5I	14500 ± 840	1.88 ± 0.12	298.1 ± 1.0	6.0 ± 1.8	0.83 ± 0.04	0.98 ± 0.05	const
SK -66 126 ^c	B5I	14440 ± 560	1.98 ± 0.20	301.0 ± 1.1	0.1 ± 2.3	1.08 ± 0.07	1.0 ± 0.06	const
HD 268654 ^c	B9I	14000 ± 620	1.74 ± 0.20	275.4 ± 1.3	21.2 ± 2.2	2.05 ± 0.14	0.99 ± 0.06	asymm
SK -68 53 ^c	B5I	13770 ± 740	2.09 ± 0.12	279.3 ± 0.9	0.8 ± 1.9	0.98 ± 0.05	0.86 ± 0.05	const
SK -66 142 ^c	B6I	13640 ± 740	2.00 ± 0.12	304.5 ± 1.1	2.8 ± 2.1	0.99 ± 0.06	0.94 ± 0.06	const
SK -66 92 ^c	B7I	13480 ± 750	1.92 ± 0.11	310.7 ± 1.1	6.3 ± 2.2	0.9 ± 0.06	0.92 ± 0.06	SB1?
HD 269801 ^c	B9I	13260 ± 670	1.73 ± 0.14	316.7 ± 0.8	0.8 ± 1.5	0.91 ± 0.04	0.98 ± 0.05	const
SK -67 198 ^c	B7I	13180 ± 790	1.85 ± 0.12	305.9 ± 1.1	0.7 ± 2.2	0.82 ± 0.05	0.91 ± 0.06	const
HD 270933 ^c	B8I	13150 ± 620	1.74 ± 0.13	296.5 ± 0.6	2.0 ± 1.2	0.99 ± 0.04	1.02 ± 0.04	const
HD 269766 ^c	B8I	12960 ± 590	1.76 ± 0.12	304.4 ± 1.0	2.7 ± 2.0	0.95 ± 0.06	0.8 ± 0.05	const
HD 41297 ^a	B8IV	12950 ± 730	3.88 ± 0.21	17.7 ± 1.3	0.3 ± 2.6	1.2 ± 0.1	1.28 ± 0.11	const
SK -70 81 ^c	B7Iab	12770 ± 1080	2.18 ± 0.21	259.9 ± 2.4	6.7 ± 4.5	1.55 ± 0.09	2.09 ± 0.12	LPV
SK -67 171 ^c	B7I	12650 ± 740	1.80 ± 0.12	309.8 ± 0.8	1.9 ± 1.7	0.99 ± 0.06	0.88 ± 0.05	const
HD 269619 ^c	B9I	12630 ± 800	1.70 ± 0.14	271.1 ± 0.6	2.6 ± 1.2	1.06 ± 0.04	0.93 ± 0.04	LPV?
GV 375 ^c	B8I	12610 ± 700	2.07 ± 0.14	300.7 ± 0.6	0.7 ± 1.3	0.84 ± 0.05	0.79 ± 0.05	const
CPD-69 490 ^c	B6I	12600 ± 760	1.70 ± 0.12	255.1 ± 0.5	3.1 ± 1.0	1.01 ± 0.04	0.89 ± 0.03	SB1?
SK -67 72 ^c	B6I	12480 ± 750	1.84 ± 0.14	300.9 ± 0.7	1.2 ± 1.4	0.88 ± 0.04	0.88 ± 0.04	const
HD 268675 ^c	B8I	12460 ± 810	1.70 ± 0.15	287.4 ± 0.8	2.8 ± 1.5	-0.84 ± 0.04	1.1 ± 0.05	asymm?
SK -67 7 ^c	B9Iab	12460 ± 760	1.83 ± 0.14	298.7 ± 0.7	2.6 ± 1.4	0.88 ± 0.04	0.88 ± 0.04	const
CPD-69 512 ^c	B9I	12300 ± 780	1.72 ± 0.13	241.5 ± 0.9	5.3 ± 1.8	0.81 ± 0.05	0.8 ± 0.05	SB1?
HD 270123 ^c	B8I	12150 ± 770	1.70 ± 0.14	292.6 ± 0.4	1.0 ± 0.9	1.01 ± 0.04	1.0 ± 0.03	const
SK -70 31 ^c	B8Iab	12060 ± 790	1.90 ± 0.15	250.9 ± 0.7	1.7 ± 1.3	0.82 ± 0.05	0.86 ± 0.05	const
HD 57970 ^a	B8III	11970 ± 720	3.73 ± 0.21	87.9 ± 1.5	4.7 ± 3.0	1.31 ± 0.07	1.08 ± 0.06	const
SK -69 250 ^c	B7I	11960 ± 730	1.70 ± 0.15	245.3 ± 0.6	8.0 ± 1.2	1.03 ± 0.05	1.12 ± 0.05	SB1
SK -69 31 ^c	B5I	11830 ± 600	1.70 ± 0.12	250.1 ± 0.5	3.6 ± 1.0	1.01 ± 0.04	0.9 ± 0.04	const
SK -70 26 ^c	B8I	11630 ± 570	1.90 ± 0.13	235.6 ± 0.5	0.4 ± 1.0	0.89 ± 0.04	0.94 ± 0.05	const
SK -67 42 ^c	B8I	11560 ± 580	1.88 ± 0.13	307.7 ± 0.4	1.0 ± 0.7	-0.9 ± 0.03	0.95 ± 0.04	const
SK -69 47 ^c	B8Ib	11540 ± 600	1.78 ± 0.14	251.1 ± 0.6	0.3 ± 1.1	0.87 ± 0.04	0.87 ± 0.04	const
SK -67 279 ^c	B7I	11330 ± 600	1.90 ± 0.15	280.4 ± 0.4	2.6 ± 0.8	0.91 ± 0.04	0.94 ± 0.04	const
SK -67 88 ^c	B8I	11220 ± 600	1.78 ± 0.13	289.8 ± 0.3	1.0 ± 0.7	0.91 ± 0.03	0.8 ± 0.02	const
HD 269721 ^c	B9I	11080 ± 600	1.70 ± 0.13	300.6 ± 0.3	2.1 ± 0.5	0.98 ± 0.02	0.95 ± 0.02	const
HD 45527 ^a	B9IV	11010 ± 600	3.88 ± 0.22	1.8 ± 1.0	2.1 ± 1.9	0.91 ± 0.05	0.9 ± 0.05	LPV?
HD 269639 ^c	B6I	11000 ± 670	1.70 ± 0.15	304.2 ± 0.4	5.2 ± 0.7	-0.93 ± 0.03	0.85 ± 0.02	SB1?
SOI 404 ^c	B9I	11000 ± 660	2.14 ± 0.17	283.2 ± 2.4	5.5 ± 0.9	1.19 ± 0.04	0.86 ± 0.03	LPV
HD 269510 ^c	B8I	11000 ± 620	1.70 ± 0.14	257.4 ± 0.2	4.0 ± 0.4	0.94 ± 0.02	0.92 ± 0.02	SB1?
SK -69 174 ^c	B9I	11000 ± 590	1.93 ± 0.15	282.8 ± 0.2	1.2 ± 0.4	0.83 ± 0.02	0.98 ± 0.02	const
SOI 247 ^c	B9.5III	11000 ± 540	2.50 ± 0.15	305.2 ± 0.1	1.3 ± 0.2	0.94 ± 0.03	0.77 ± 0.02	const
SK -70 77 ^c	B9Ib	11000 ± 530	2.02 ± 0.15	235.7 ± 0.2	1.2 ± 0.4	0.94 ± 0.02	1.05 ± 0.02	const
SK -68 152 ^c	B8I	11000 ± 530	2.01 ± 0.13	271.0 ± 0.2	1.0 ± 0.4	0.78 ± 0.02	0.82 ± 0.02	const
SK -67 151 ^c	B9Ib	11000 ± 510	2.24 ± 0.15	303.3 ± 0.2	0.2 ± 0.4	0.82 ± 0.02	-0.94 ± 0.02	const
SOI 574 ^c	B9II	11000 ± 500	2.20 ± 0.13	245.1 ± 0.2	2.1 ± 0.3	1.04 ± 0.02	0.87 ± 0.02	SB1
SOI 166	B9Ib	-	-	9.6 ± 3.4	1.9 ± 6.7	0.89 ± 0.08	0.92 ± 0.08	const
FEROS								
HD 269676 ^b	O7	47480 ± 3790	3.56 ± 0.20	267.6 ± 10.7	3.7 ± 20.9	1.26 ± 0.43	1.53 ± 0.5	const
HD 269321 ^b	B5I	20000 ± 800	2.13 ± 0.20	281.5 ± 0.9	11.0 ± 2.0	1.14 ± 0.07	1.0 ± 0.06	SB1?asymm?
HD 269440 ^b	B1I	20000 ± 1780	2.33 ± 0.23	314.6 ± 1.3	1.2 ± 2.4	1.03 ± 0.05	1.45 ± 0.06	asymm?
HD 269660 ^b	B2I	19460 ± 700	2.00 ± 0.20	246.1 ± 0.9	4.5 ± 1.8	1.12 ± 0.05	1.2 ± 0.05	const
HD 269700 ^c	B1.5	18000 ± 780	1.92 ± 0.20	281.7 ± 2.4	19.7 ± 4.8	6.06 ± 0.87	4.68 ± 0.63	asymm
HD 269832 ^b	B6I	17580 ± 730	1.92 ± 0.20	261.5 ± 0.9	3.7 ± 1.6	1.14 ± 0.06	1.16 ± 0.05	const
HD 268798 ^b	B2I	17470 ± 1660	2.08 ± 0.21	286.7 ± 1.3	2.4 ± 2.7	1.68 ± 0.09	1.38 ± 0.07	SB1?asymm?
HD 268726 ^b	B3I	17290 ± 1490	2.05 ± 0.21	310.7 ± 1.4	4.5 ± 2.9	1.47 ± 0.08	1.57 ± 0.1	const
HD 269992 ^b	B2I	16980 ± 1980	2.07 ± 0.23	252.2 ± 1.2	5.1 ± 2.6	1.56 ± 0.08	1.44 ± 0.08	asymm?
HD 268654 ^b	B9I	16580 ± 880	1.94 ± 0.20	259.6 ± 1.2	7.4 ± 2.1	0.78 ± 0.05	0.96 ± 0.05	asymm?
HD 269997 ^b	B2.5Iab	16500 ± 910	1.98 ± 0.20	262.2 ± 1.4	7.3 ± 2.8	0.91 ± 0.06	0.95 ± 0.05	SB1?
HD 268907 ^b	B5I	16430 ± 950	1.96 ± 0.20	304.5 ± 0.9	4.0 ± 1.8	0.95 ± 0.05	0.97 ± 0.05	const
HD 268729 ^b	B5I	16430 ± 930	1.98 ± 0.20	248.1 ± 1.1	9.5 ± 2.2	0.8 ± 0.05	0.73 ± 0.04	SB1

Table A.1. continued.

Object name	Spectral class	T_{eff} (K)	$\log g$ (dex)	RV_1 (km s^{-1})	ΔRV	Asymmetry_1	Asymmetry_2	Variability
HD 269786 ^c	B1I	16000 ± 780	1.95 ± 0.20	292.1 ± 1.4	5.9 ± 3.8	1.9 ± 0.12	1.78 ± 0.2	asymm
HD 268653 ^c	B2I	16000 ± 1000	1.96 ± 0.20	308.1 ± 1.8	9.1 ± 3.4	1.08 ± 0.08	1.27 ± 0.08	SB1?asymm?
HD 269859 ^c	B0I	16000 ± 1000	1.94 ± 0.20	257.9 ± 1.7	23.9 ± 3.6	2.31 ± 0.18	2.75 ± 0.22	asymm
HD 269145 ^c	B5I	15960 ± 770	1.98 ± 0.20	318.0 ± 1.2	0.1 ± 2.4	1.17 ± 0.07	1.16 ± 0.07	const
HD 271163 ^c	B3I	15760 ± 770	2.00 ± 0.20	304.6 ± 2.5	0.1 ± 4.0	1.13 ± 0.13	0.99 ± 0.07	const
HD 270949 ^b	B5I	15730 ± 1000	1.96 ± 0.20	295.7 ± 1.3	11.1 ± 2.7	0.99 ± 0.06	0.99 ± 0.07	SB1?asymm?
HD 269854 ^c	B5I	15300 ± 790	1.98 ± 0.20	291.2 ± 1.3	0.6 ± 2.6	1.0 ± 0.06	0.91 ± 0.06	const
HD 269606 ^c	B5I	15290 ± 760	1.99 ± 0.20	292.7 ± 1.2	10.9 ± 2.4	0.83 ± 0.05	0.88 ± 0.05	SB1?asymm?
HD 269644 ^c	B6I	15170 ± 770	1.96 ± 0.20	312.9 ± 1.0	5.8 ± 2.0	1.06 ± 0.06	0.94 ± 0.05	const
HD 269593 ^c	B7I	15020 ± 770	1.92 ± 0.20	316.4 ± 1.2	5.6 ± 2.4	0.92 ± 0.05	0.88 ± 0.05	const
HD 269238 ^c	B6I	14600 ± 750	1.86 ± 0.20	248.8 ± 0.7	6.5 ± 1.5	0.98 ± 0.05	0.96 ± 0.05	SB1?
CD-65 288 ^c	B6I	14510 ± 790	1.90 ± 0.20	288.3 ± 1.1	4.0 ± 2.3	0.91 ± 0.05	0.86 ± 0.06	const
HD 269766 ^c	B8I	13940 ± 750	1.86 ± 0.20	303.1 ± 1.0	5.2 ± 2.1	0.8 ± 0.04	1.01 ± 0.07	asymm?
HD 269801 ^c	B9I	13830 ± 720	1.76 ± 0.20	317.6 ± 0.8	1.4 ± 1.5	-1.13 ± 0.07	-1.0 ± 0.05	const
HD 269619 ^c	B9I	13660 ± 720	1.78 ± 0.20	269.1 ± 0.9	1.9 ± 1.8	0.86 ± 0.05	0.79 ± 0.04	LPV?
HD 53048 ^c	B5III	13590 ± 2350	2.48 ± 0.36	277.2 ± 8.3	10.9 ± 16.8	1.11 ± 0.2	1.1 ± 0.2	const
HD 268675 ^c	B8I	13430 ± 700	1.78 ± 0.20	285.1 ± 0.7	10.2 ± 1.5	0.81 ± 0.04	1.06 ± 0.06	SB1asymm?
HD 270933 ^c	B8I	13300 ± 700	1.79 ± 0.20	291.7 ± 0.9	1.6 ± 1.7	0.86 ± 0.05	1.01 ± 0.05	const
HD 61950 ^c	B8III	12830 ± 2470	2.50 ± 0.45	314.8 ± 4.7	189.6 ± 10.5	1.4 ± 0.31	1.66 ± 0.46	asymm?
HD 270296 ^c	B6I	12570 ± 1280	1.70 ± 0.20	287.1 ± 1.0	2.4 ± 2.3	0.94 ± 0.06	0.98 ± 0.08	const
HD 269684 ^c	B9I	12480 ± 1240	1.70 ± 0.20	327.0 ± 0.8	3.4 ± 1.7	-0.98 ± 0.06	-1.0 ± 0.06	const
HD 269195 ^c	B9I	12300 ± 1250	1.70 ± 0.22	293.8 ± 1.0	5.6 ± 1.8	0.95 ± 0.07	0.95 ± 0.06	SB1?
HD 270123 ^c	B8I	12240 ± 1280	1.70 ± 0.22	289.0 ± 0.8	1.2 ± 1.6	0.79 ± 0.05	0.77 ± 0.05	const
HD 269639 ^c	B7I	11600 ± 960	1.70 ± 0.20	305.5 ± 0.6	5.6 ± 1.2	1.18 ± 0.06	0.93 ± 0.05	SB1?
HD 269510 ^c	B8I	11580 ± 930	1.70 ± 0.19	264.4 ± 0.5	7.5 ± 1.0	1.12 ± 0.04	0.89 ± 0.04	SB1?
HD 269721 ^c	B9I	11330 ± 970	1.70 ± 0.20	300.0 ± 0.5	3.5 ± 1.1	0.9 ± 0.04	0.9 ± 0.05	const
HD 269664 ^c	B9I	11120 ± 930	1.70 ± 0.19	248.3 ± 0.4	3.7 ± 0.8	0.95 ± 0.04	0.98 ± 0.04	SB1?asymm?
HD 268835	—	—	—	—	—	—	—	const
HD 269582	—	—	—	—	—	—	—	const
HD 268718	—	—	—	—	—	—	—	const

Appendix B: Results of spectral line profiles characterisation

Table B.1. Characteristics of the spectral line profile broadening in the combined UVES and FEROS sample.

Object name	$v \sin i_{\text{SP}}$	$v \sin i_{\text{FT}}$	$\Theta (a_T = 0.5)$ (km s^{-1})	$\Theta (a_T \text{ varied})$	a_T
UVES					
SK -71 51	170.5± 23.4	131.3± 18.2	183.8± 189.0	-	-
HT 83 alf	269.0± 24.3	202.6± 7.8	28.0± 117.5	38.2± 370.6	0.02± 0.11
BI 42	141.0± 18.3	124.3± 24.2	67.8± 232.7	53.3± 136.2	0.54± 0.07
HD 269525	174.0± 19.8	102.6± 8.4	145.2± 70.5	140.1± 38.3	0.11± 0.09
SK -66 138	72.5± 11.7	66.3± 9.4	84.4± 87.3	87.6± 802.0	0.47± 0.44
RMC 95	83.5± 12.2	71.7± 7.2	107.6± 12.1	106.6± 134.9	0.16± 0.14
RMC 93	139.5± 16.2	144.1± 20.1	50.5± 63.6	57.6± 56.1	0.43± 0.08
BI 188	99.0± 15.2	79.6± 10.0	85.3± 156.0	87.0± 51.6	0.45± 0.07
HD 269769	107.0± 13.8	80.2± 17.5	73.7± 56.1	69.5± 18.4	0.53± 0.03
SK -70 13	93.5± 14.0	60.3± 4.5	98.3± 25.8	101.3± 45.6	0.63± 0.14
RMC 97	84.0± 12.3	63.8± 12.2	124.5± 20.9	127.0± -	0.95± 1.24
SK -66 15	62.5± 10.0	63.6± 12.8	58.0± 43.4	55.7± 233.4	0.72± 0.17
SK -69 180	56.5± 8.4	48.2± 4.6	49.5± 16.9	47.6± 14.6	0.75± 0.03
SK -67 54	60.5± 9.5	65.5± 7.6	43.1± 29.1	36.6± 13.8	0.47± 0.03
SK -69 275	63.5± 9.5	61.7± 9.0	59.9± 41.1	57.0± 12.9	0.67± 0.04
MCPS 082.95108-69.23933	53.5± 8.0	49.6± 9.2	47.8± 4.2	48.0± 10.4	0.59± 0.05
HD 269700	101.5± 13.9	67.7± 19.1	59.8± 4.5	59.7± 21.9	0.62± 0.07
CPD-69 457	68.5± 10.8	68.3± 12.7	88.9± 23.8	81.3± -	0.59± 0.68
SK -68 147	51.0± 8.2	44.3± 9.4	51.2± 15.9	54.0± 9.1	0.69± 0.06
Dachs LMC 2-19	62.0± 9.5	63.1± 6.7	37.4± 12.7	36.9± 181.8	0.46± 0.17
HD 269314	95.5± 14.3	78.6± 12.2	70.9± 67.6	66.3± 25.0	0.63± 0.05
CPD-69 445	68.0± 10.4	66.8± 11.9	56.0± 38.2	51.4± 14.9	0.62± 0.04
SK -69 256	62.5± 9.9	66.9± 12.1	52.5± 28.0	45.8± 27.4	0.74± 0.04
RMC 142	65.0± 10.4	55.2± 8.7	52.2± 27.4	54.7± 11.7	0.73± 0.06
HD 269859	52.5± 8.5	41.9± 5.6	61.2± 14.2	57.9± 8.4	0.6± 0.07
HD 270754	55.5± 9.0	56.6± 8.2	44.4± 5.2	40.5± 8.5	0.56± 0.04
HD 270196	54.5± 8.5	53.6± 10.6	52.8± 2.2	47.5± 6.9	0.7± 0.03
SK -67 46	52.5± 8.1	46.2± 10.5	51.3± 5.2	52.4± 10.0	0.59± 0.04
SK -69 167	58.5± 9.2	51.6± 13.9	61.5± 8.0	56.1± 13.1	0.75± 0.04
HD 269786	58.0± 9.2	56.9± 10.4	64.2± 11.4	66.0± 5.6	0.89± 0.03
SK -67 76	82.5± 14.2	61.6± 8.4	61.8± 9.0	63.5± 363.1	0.46± 0.22
HD 269655	73.0± 11.0	64.2± 15.7	60.0± 14.4	56.4± 193.5	0.68± 0.12
SK -69- 157	72.5± 12.0	55.4± 13.7	70.4± 58.8	70.3± 134.0	0.47± 0.09
HD 269660	47.5± 7.4	49.6± 6.5	54.0± 10.1	59.6± 6.0	0.99± 0.05
SK -69 68	70.5± 10.4	72.5± 7.2	59.8± 29.8	56.4± 16.2	0.24± 0.03
HD 268809	58.5± 8.7	50.1± 9.8	55.5± 34.0	52.1± 203.6	0.7± 0.16
LH 47-373A	61.5± 9.2	65.4± 4.2	47.4± 9.3	44.2± 156.4	0.56± 0.13
HD 268623	59.0± 9.4	66.7± 9.2	53.2± 20.2	54.9± 14.4	0.87± 0.03
SK -68 17	44.0± 7.2	42.1± 6.8	51.9± 11.7	47.7± 7.3	0.63± 0.04
W61 27-5	56.0± 8.4	45.0± 3.8	54.6± 14.3	43.4± 15.8	0.58± 0.06
HD 268798	56.0± 8.8	49.2± 7.8	55.2± 9.4	49.2± 82.1	0.72± 0.06
CPD-68 309	46.5± 7.8	50.4± 4.9	21.7± 4.1	23.1± 7.0	0.91± 0.1
SK -68 27	55.0± 9.9	41.5± 5.2	47.2± 11.7	45.9± 3.3	0.63± 0.02
HD 269845	48.5± 8.3	43.6± 7.7	54.2± 5.4	44.4± 2.2	0.62± 0.01
SK -68 2	55.5± 10.6	38.4± 10.4	46.9± 5.4	45.6± 75.5	0.66± 0.08
HD 268653	54.0± 9.0	39.3± 8.4	46.0± 2.5	47.5± 19.5	0.5± 0.08
HD 269992	45.5± 8.2	48.3± 9.3	48.0± 6.4	53.0± 64.8	0.99± 0.13
HD 269997	44.5± 9.3	46.3± 6.9	45.0± 2.2	51.5± 2.6	0.88± 0.02
HD 269101	46.0± 8.8	44.4± 8.9	36.4± 5.2	32.3± 17.3	0.84± 0.11
SK -67 133	53.5± 10.4	40.3± 7.7	40.3± 4.9	38.0± 3.7	0.61± 0.01
HD 268729	53.5± 10.4	52.8± 8.1	39.2± 3.6	35.2± 20.3	0.69± 0.09
HD 271213	54.0± 9.6	44.8± 7.9	46.0± 4.6	46.9± 4.5	0.7± 0.01
HD 270949	67.0± 11.5	45.7± 6.3	38.6± 4.8	38.4± 42.4	0.51± 0.14
HD 269145	58.5± 11.2	46.5± 4.6	39.8± 1.5	36.6± 20.0	0.73± 0.08
HD 269920	55.5± 10.7	41.7± 6.1	45.3± 3.0	43.7± 3.0	0.73± 0.01
HD 269854	54.5± 10.4	42.4± 4.8	27.2± 2.0	40.3± 4.1	0.71± 0.01
SK -70 53	40.5± 9.0	29.8± 5.6	43.2± 5.1	43.0± 1.3	0.5± 0.01
SK -67 275	63.5± 12.1	54.2± 3.3	39.9± 2.8	38.8± 41.8	0.53± 0.12
SK -67 283	46.5± 11.9	38.6± 5.3	34.6± 1.0	32.8± 3.6	0.53± 0.02
HD 47620	23.5± 10.0	34.3± -	-	-	-
SK -66 125	36.5± 11.5	34.2± 3.9	25.0± 2.5	25.2± 2.3	0.6± 0.01

Table B.1. continued.

Object name	$v \sin i_{\text{SP}}$	$v \sin i_{\text{FT}}$	$\Theta (a_T = 0.5)$ (km s $^{-1}$)	$\Theta (a_T \text{ varied})$	a_T
HD 269644	57.5 ± 12.0	47.7 ± 5.2	28.9 ± 2.2	25.0 ± 5.6	0.75 ± 0.01
SK -67 127	44.5 ± 11.9	33.8 ± 5.5	36.2 ± 5.9	34.3 ± 11.1	0.63 ± 0.06
HD 268907	72.0 ± 14.0	40.6 ± 3.7	44.4 ± 2.5	33.1 ± 2.8	1.0 ± 0.01
SK -66 126	46.5 ± 12.8	36.5 ± 4.9	30.8 ± 4.1	28.9 ± 3.8	0.62 ± 0.01
HD 268654	112.5 ± 21.0	43.4 ± 4.6	24.9 ± 3.4	34.6 ± 14.0	0.63 ± 0.07
SK -68 53	47.5 ± 11.5	30.4 ± 4.1	45.9 ± 1.9	32.8 ± 1.1	1.0 ± 0.04
SK -66 142	49.0 ± 11.4	33.2 ± -	-	-	-
SK -66 92	51.5 ± 11.0	30.8 ± 3.2	31.8 ± 1.1	33.6 ± 3.9	0.42 ± 0.01
HD 269801	71.5 ± 14.2	36.7 ± 3.4	38.1 ± 3.3	43.4 ± 1.1	0.65 ± 0.03
SK -67 198	56.0 ± 13.2	39.5 ± 4.1	34.7 ± 2.4	29.5 ± 2.5	0.61 ± 0.01
HD 270933	57.0 ± 11.8	35.1 ± -	-	-	-
HD 269766	44.5 ± 11.9	37.6 ± 6.1	30.9 ± 1.5	30.2 ± 12.2	0.58 ± 0.07
HD 41297	29.5 ± 11.6	32.2 ± 5.3	8.4 ± 2.5	5.5 ± 10.4	0.73 ± 0.65
SK -70 81	105.0 ± 24.0	101.5 ± 4.2	29.8 ± 4.1	26.8 ± 8.6	0.05 ± 0.01
SK -67 171	47.5 ± 11.5	30.6 ± 5.2	27.1 ± 4.0	27.3 ± 5.2	0.46 ± 0.03
HD 269619	52.5 ± 13.0	37.0 ± 2.9	35.4 ± 2.9	35.1 ± 6.0	0.53 ± 0.02
GV 375	43.5 ± 9.4	25.5 ± 3.9	23.7 ± 0.3	22.3 ± 2.8	0.64 ± 0.04
CPD-69 490	45.0 ± 10.9	28.1 ± 3.6	35.1 ± 2.3	30.0 ± 0.5	0.54 ± 0.03
SK -67 72	46.5 ± 11.8	31.9 ± 2.2	31.9 ± 2.1	28.6 ± 0.5	0.74 ± 0.02
HD 268675	53.0 ± 11.6	34.5 ± 3.8	48.0 ± 0.2	47.2 ± 4.2	0.63 ± 0.03
SK -67 7	46.5 ± 11.8	19.2 ± -	35.4 ± 2.6	26.0 ± 4.6	0.74 ± 0.02
CPD-69 512	48.5 ± 12.0	29.0 ± 4.2	34.3 ± 4.8	31.3 ± 0.9	0.59 ± 0.04
HD 270123	45.0 ± 10.6	30.0 ± 5.0	30.3 ± 1.7	-	-
SK -70 31	33.0 ± 10.6	27.8 ± 2.8	27.2 ± 0.2	25.0 ± 0.5	0.46 ± 0.03
HD 57970	61.5 ± 22.0	67.8 ± -	-	-	-
SK -69 250	34.5 ± 11.8	34.8 ± 5.6	27.9 ± 3.0	28.6 ± 0.7	0.69 ± 0.05
SK -69 31	44.0 ± 9.7	32.9 ± 6.4	32.2 ± 1.5	30.8 ± 4.4	0.57 ± 0.01
SK -70 26	39.5 ± 9.8	27.4 ± 3.9	21.1 ± 2.0	21.4 ± 2.0	0.63 ± 0.03
SK -67 42	41.5 ± 9.0	21.4 ± 5.6	24.4 ± 0.2	25.3 ± 4.1	0.46 ± 0.02
SK -69 47	42.5 ± 9.5	31.9 ± -	-	-	-
SK -67 279	23.0 ± 10.2	23.8 ± 3.5	21.2 ± 0.2	20.5 ± 2.2	0.56 ± 0.03
SK -67 88	44.0 ± 10.0	23.6 ± 2.3	32.0 ± 1.2	35.5 ± 1.1	0.44 ± 0.01
HD 269721	40.0 ± 8.9	32.6 ± 4.0	27.6 ± 0.1	26.6 ± 4.2	0.57 ± 0.01
HD 45527	44.5 ± 13.0	48.2 ± 2.9	44.5 ± 2.1	52.4 ± 22.2	1.0 ± 0.04
HD 269639	26.5 ± 15.0	34.8 ± 5.5	26.0 ± 1.9	-	-
SOI 404	44.0 ± 11.4	38.0 ± 3.1	27.6 ± 0.4	26.2 ± 0.8	0.54 ± 0.06
HD 269510	39.0 ± 10.6	29.5 ± 5.1	30.7 ± 0.1	30.9 ± 0.2	0.55 ± 0.01
SK -69 174	18.0 ± 12.0	29.0 ± 4.2	21.9 ± 1.3	18.8 ± 5.2	0.66 ± 0.02
SOI 247	36.0 ± 8.9	18.2 ± -	-	-	-
SK -70 77	34.5 ± 8.4	22.8 ± -	-	-	-
SK -68 152	34.0 ± 8.0	14.4 ± -	-	-	-
SK -67 151	8.0 ± 19.8	21.8 ± -	-	-	-
SOI 574	32.0 ± 7.2	22.2 ± -	-	-	-
SOI 166	-	138.8 ± 28.0	200.0 ± 18142.1	199.9 ± 6207.7	0.11 ± 1.53
FEROS					
HD 269676	181.5 ± 33.3	-	-	-	-
HD 269321	78.0 ± 16.4	35.3 ± 7.6	30.7 ± 7.7	27.5 ± 29.3	0.69 ± 0.08
HD 269440	51.5 ± 11.0	54.8 ± 10.0	24.9 ± 59.8	29.4 ± 173.4	1.0 ± 0.46
HD 269660	50.0 ± 11.5	47.5 ± 10.0	52.2 ± 12.5	47.2 ± 255.3	0.86 ± 0.25
HD 269700	80.5 ± 19.5	43.4 ± 5.1	100.0 ± 35.0	96.0 ± 251.6	0.11 ± 1.73
HD 269832	96.0 ± 21.3	49.7 ± 19.5	32.6 ± 4.7	20.8 ± 3.9	0.99 ± 0.03
HD 268798	57.5 ± 13.6	51.3 ± 12.7	45.6 ± 48.3	47.9 ± 120.7	0.54 ± 0.12
HD 268726	60.0 ± 14.2	48.4 ± 15.4	56.1 ± 53.9	55.4 ± 475.4	0.72 ± 0.5
HD 269992	51.0 ± 12.5	43.5 ± 3.3	52.6 ± 11.6	52.2 ± 11.3	0.47 ± 0.07
HD 268654	80.0 ± 18.7	37.5 ± 5.7	32.4 ± 8.4	31.5 ± 10.4	0.64 ± 0.03
HD 269997	50.5 ± 12.0	41.6 ± 11.5	42.8 ± 36.0	29.5 ± 136.3	0.63 ± 0.3
HD 268907	64.5 ± 15.3	38.5 ± 5.8	24.0 ± 7.7	26.3 ± 75.9	0.39 ± 0.1
HD 268729	55.5 ± 13.2	40.7 ± 10.5	23.4 ± 16.9	35.4 ± 6.7	0.6 ± 0.02
HD 269786	64.0 ± 17.8	49.8 ± 14.8	63.3 ± 132.8	72.3 ± 44.7	0.72 ± 0.15
HD 268653	65.0 ± 17.6	61.7 ± 14.1	47.3 ± 66.0	51.0 ± 591.1	0.87 ± 0.46
HD 269859	67.5 ± 17.4	47.4 ± 5.6	85.4 ± 18.3	95.1 ± 185.3	0.7 ± 0.4
HD 269145	65.0 ± 17.8	45.3 ± 3.6	36.2 ± 21.3	37.7 ± 170.2	0.67 ± 0.22
HD 271163	57.5 ± 17.5	47.1 ± 5.8	11.9 ± 61.8	14.1 ± 787.2	0.15 ± 0.65
HD 270949	55.5 ± 13.2	39.6 ± 6.9	32.6 ± 11.3	30.6 ± 6.9	0.52 ± 0.08
HD 269854	72.0 ± 19.6	30.5 ± 9.7	34.4 ± 18.3	34.1 ± 54.0	0.37 ± 0.11
HD 269606	56.0 ± 16.8	42.3 ± 6.6	30.9 ± 6.6	23.7 ± 5.8	0.82 ± 0.04

Table B.1. continued.

Object name	$v \sin i_{\text{SP}}$	$v \sin i_{\text{FT}}$	$\Theta (a_T = 0.5)$ (km s $^{-1}$)	$\Theta (a_T \text{ varied})$	a_T
HD 269644	62.0 ± 17.6	38.5 ± 3.9	26.0 ± 13.8	28.1 ± 102.2	0.45 ± 0.16
HD 269593	55.0 ± 17.1	35.0 ± 6.4	36.2 ± 13.3	30.6 ± 66.4	0.13 ± 0.06
HD 269238	64.5 ± 20.0	37.0 ± 5.4	31.5 ± 4.9	30.3 ± 3.6	0.58 ± 0.01
CD-65 288	59.5 ± 19.0	33.4 ± 6.8	30.1 ± 3.0	32.9 ± 28.7	0.37 ± 0.05
HD 269766	58.0 ± 18.0	36.0 ± 5.3	26.9 ± 7.3	27.5 ± 13.2	0.38 ± 0.1
HD 269801	68.5 ± 20.3	39.7 ± 2.3	18.6 ± 3.0	24.1 ± 3.2	0.55 ± 0.02
HD 269619	62.0 ± 19.6	36.9 ± 4.4	33.9 ± 5.8	30.9 ± 24.8	0.81 ± 0.05
HD 53048	344.0 ± 73.6	231.1 ± 68.8	82.5 ± 1272.7	$69.5 \pm -$	0.48 ± 0.32
HD 268675	52.5 ± 17.5	$36.9 \pm -$	-	-	-
HD 270933	52.5 ± 17.5	28.7 ± 6.8	26.5 ± 4.4	32.3 ± 10.8	0.19 ± 0.1
HD 61950	344.0 ± 74.0	298.9 ± 63.5	40.6 ± 146.8	51.9 ± 753.3	0.75 ± 1.44
HD 270296	53.5 ± 19.5	36.0 ± 4.9	30.2 ± 2.5	31.5 ± 3.6	0.48 ± 0.01
HD 269684	49.0 ± 17.8	38.1 ± 2.5	24.1 ± 4.6	22.1 ± 31.4	0.6 ± 0.1
HD 269195	48.0 ± 18.1	33.8 ± 3.1	27.7 ± 3.5	22.3 ± 13.3	0.41 ± 0.11
HD 270123	52.0 ± 17.8	38.3 ± 3.3	21.3 ± 5.6	23.5 ± 3.2	0.74 ± 0.04
HD 269639	43.5 ± 14.5	32.0 ± 7.0	18.7 ± 5.6	18.0 ± 31.4	0.42 ± 0.12
HD 269510	38.5 ± 15.4	36.5 ± 3.9	15.3 ± 3.4	12.9 ± 3.8	0.75 ± 0.14
HD 269721	43.0 ± 16.0	33.3 ± 5.9	19.6 ± 3.5	20.6 ± 15.7	0.55 ± 0.06
HD 269664	35.5 ± 15.2	36.3 ± 2.3	11.9 ± 8.1	5.9 ± 12.6	0.71 ± 0.72
HD 268835	-	-	-	-	-
HD 269582	-	-	-	-	-
HD 268718	-	36.7 ± 12.4	-	-	-

Appendix C: Results of Monte Carlo simulations of broadened line profiles

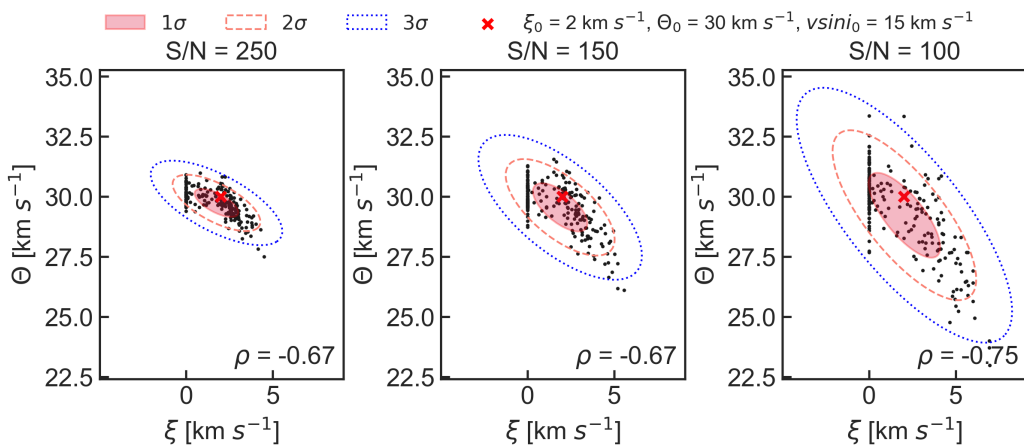


Fig. C.1. Results of Monte Carlo simulations on synthetic profiles of Mg II 4481 Å line with artificial noise (left panel: S/N = 250, middle panel: S/N = 150, and right panel: S/N = 100) with 1-, 2- and 3- σ confidence ellipses. Correlation coefficients ρ are indicated in right corner of each panel. $v \sin i$ is fixed, while Θ and ξ are optimised. The red crosses mark true parameters of the synthetic profiles.

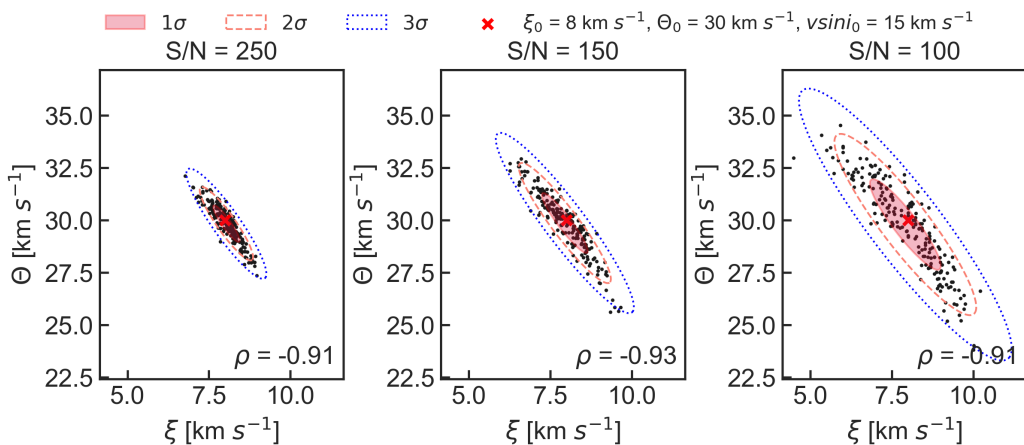


Fig. C.2. Same as Fig. C.1 for another set of parameters $v \sin i$, ξ , and Θ in the synthetic profile.

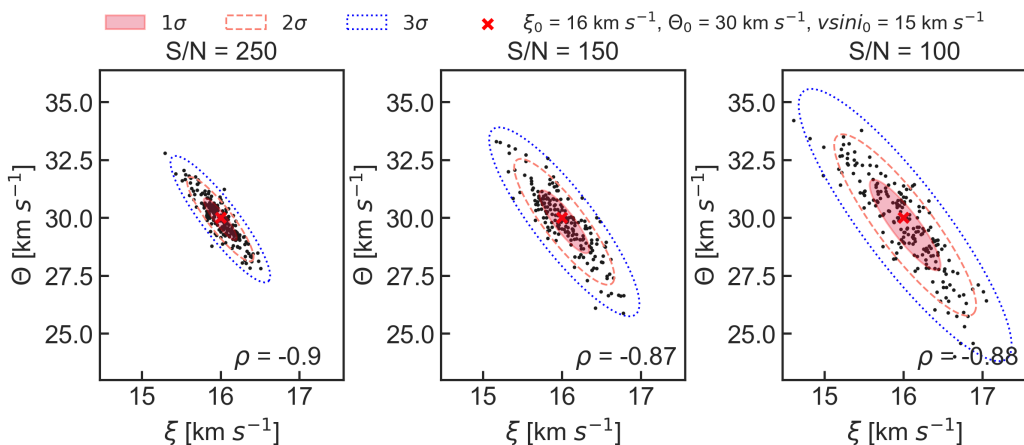


Fig. C.3. Same as Fig. C.1 for another set of parameters $v \sin i$, ξ , and Θ in the synthetic profile.

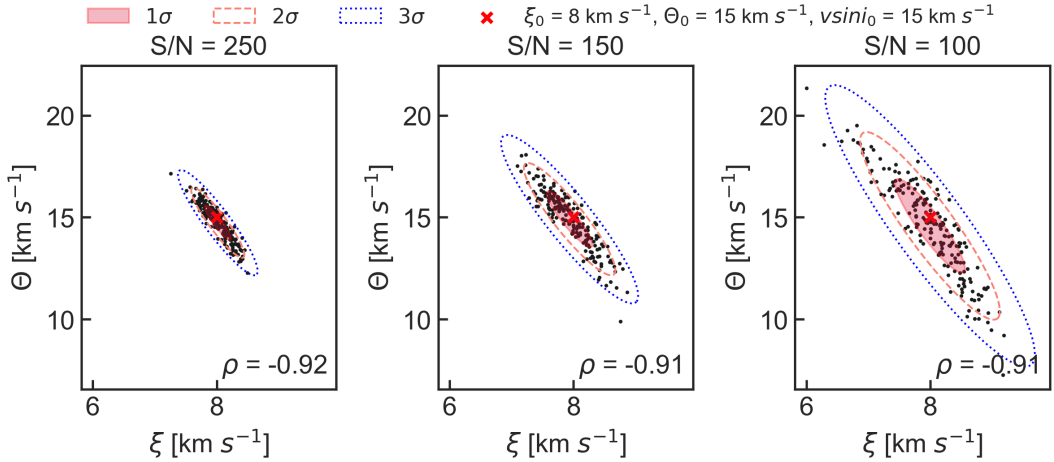


Fig. C.4. Same as Fig. C.1 for another set of parameters $v \sin i$, ξ , and Θ in the synthetic profile.

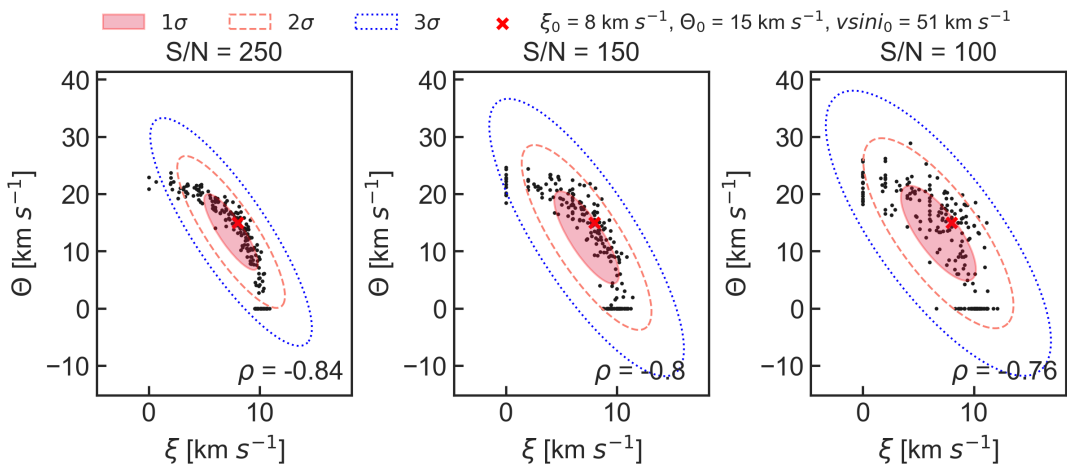


Fig. C.5. Same as Fig. C.1 for another set of parameters $v \sin i$, ξ , and Θ in the synthetic profile.

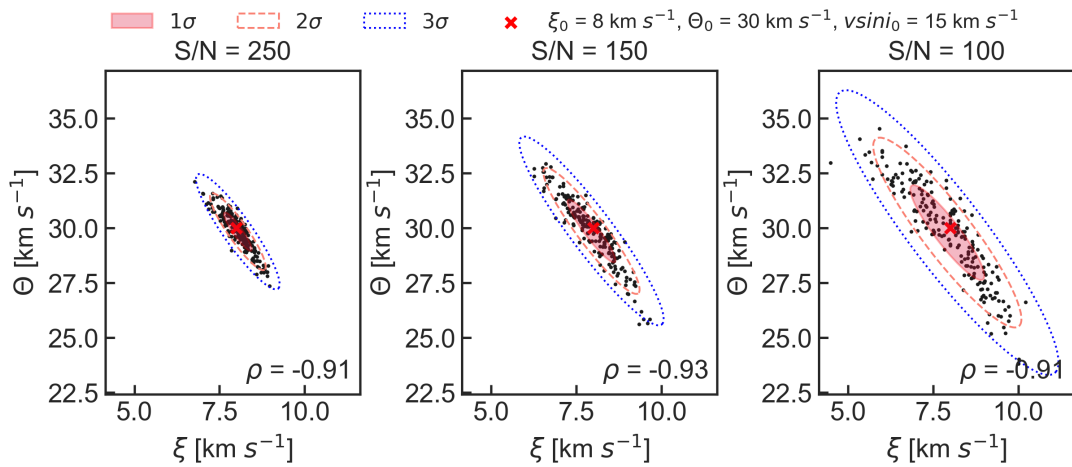


Fig. C.6. Same as Fig. C.1 for another set of parameters $v \sin i$, ξ , and Θ in the synthetic profile.

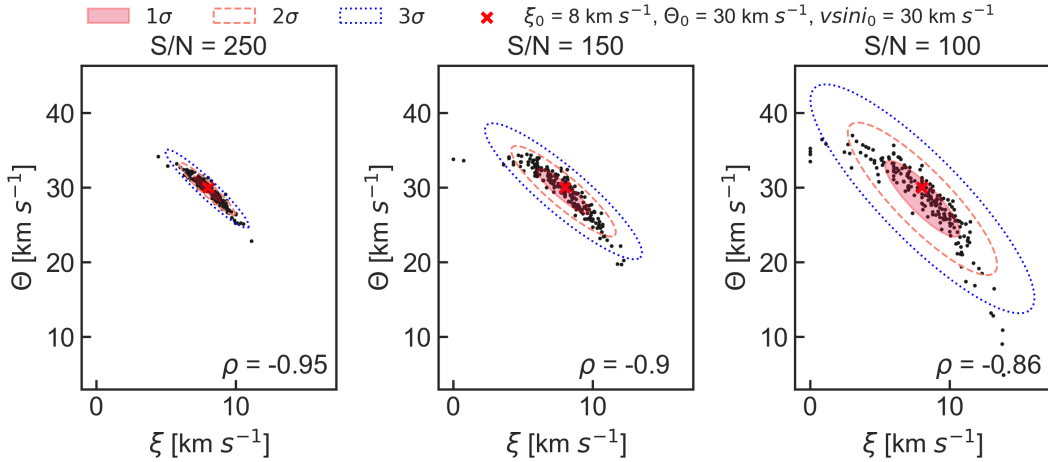


Fig. C.7. Same as Fig. C.1 for another set of parameters $v \sin i$, ξ , and Θ in the synthetic profile.

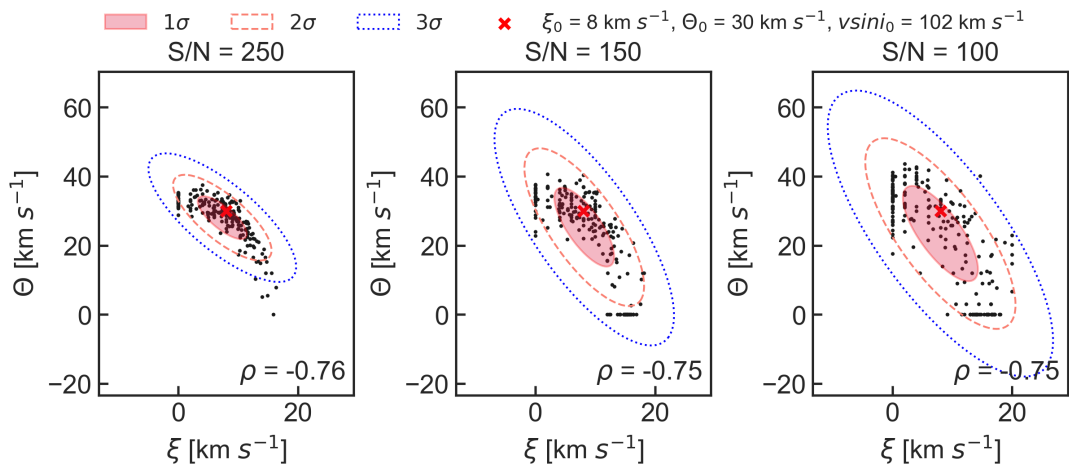


Fig. C.8. Same as Fig. C.1 for another set of parameters $v \sin i$, ξ , and Θ in the synthetic profile.

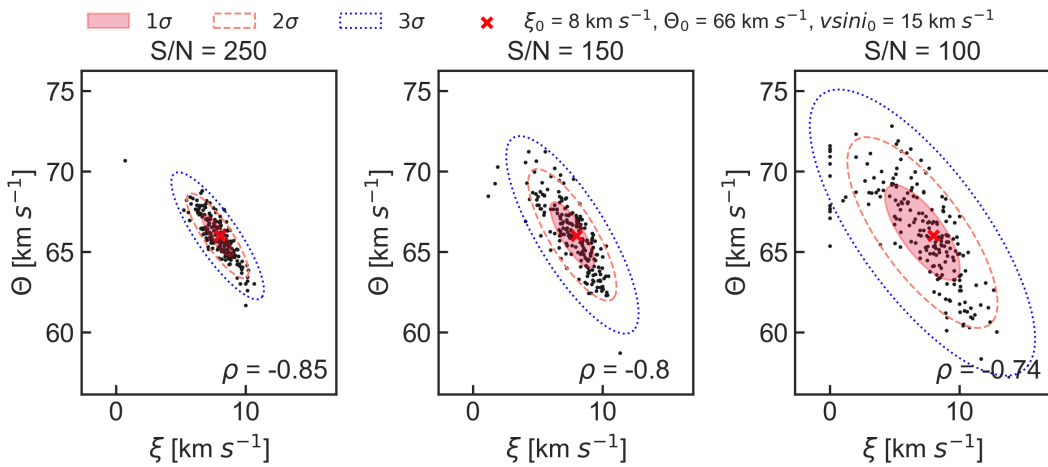


Fig. C.9. Same as Fig. C.1 for another set of parameters $v \sin i$, ξ , and Θ in the synthetic profile.

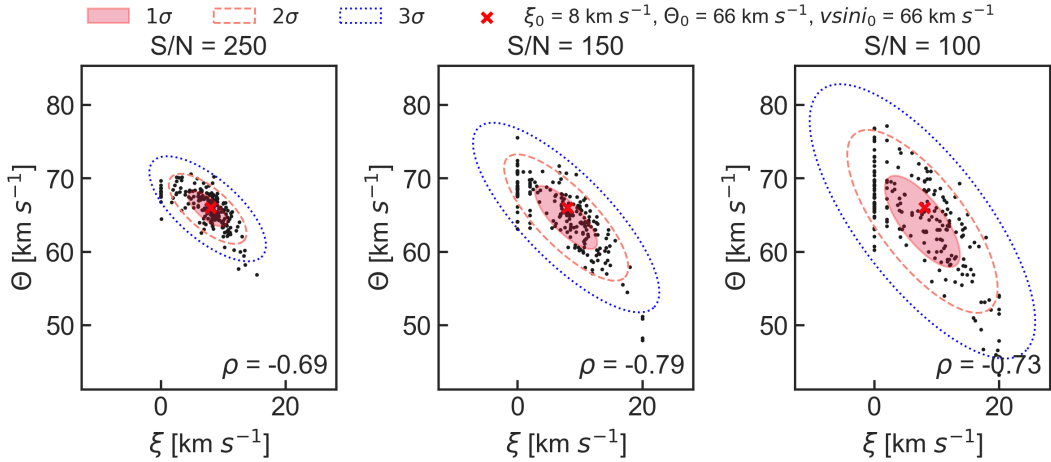


Fig. C.10. Same as Fig. C.1 for another set of parameters $v \sin i$, ξ , and Θ in the synthetic profile.

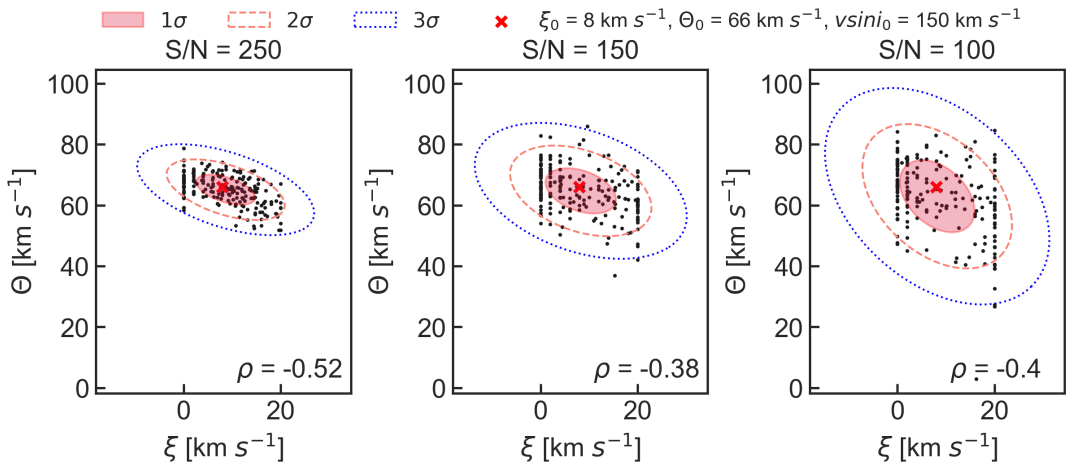


Fig. C.11. Same as Fig. C.1 for another set of parameters $v \sin i$, ξ , and Θ in the synthetic profile.

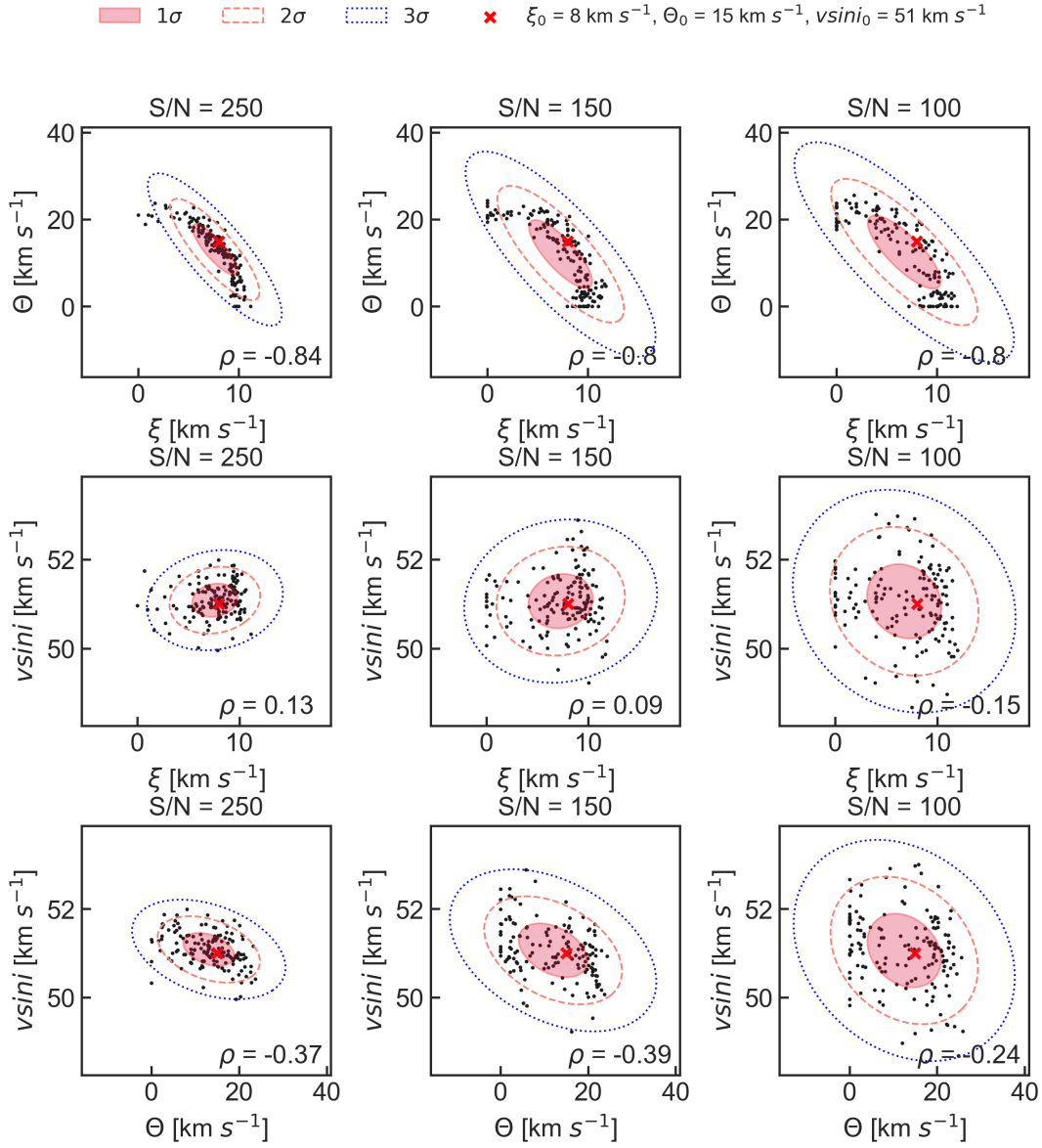


Fig. C.12. Same as Fig. C.1 but $v \sin i$ is optimised as well as ξ and Θ , resulting in three free parameters.

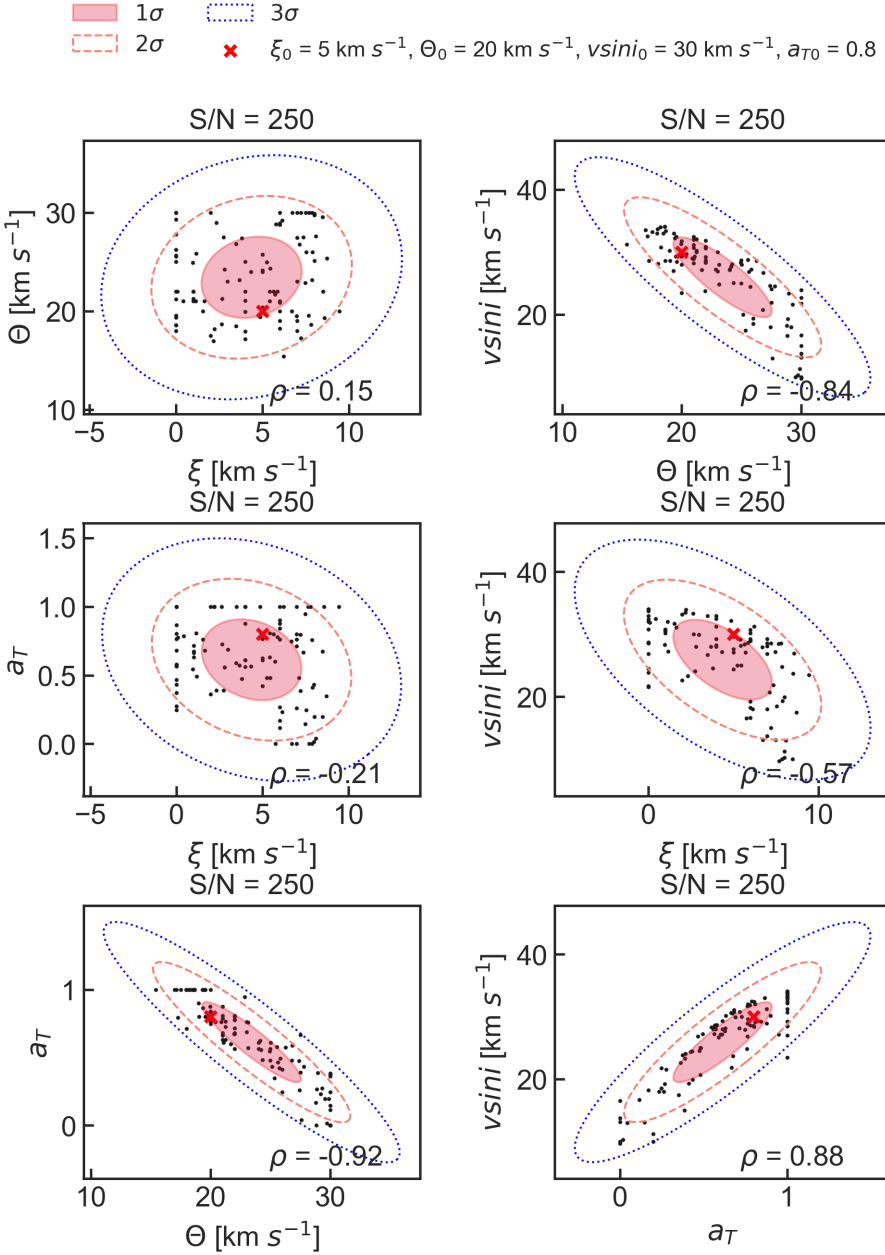


Fig. C.13. Same as Fig. C.1 but $v \sin i$ and a_T are optimised as well as ξ and Θ , resulting in four free parameters. Only the results for S/N=250 are shown.